Contrib Mineral Petrol (2017) 172:11
DOI 10.1007/s00410-017-1328-2

ORIGINAL PAPER

Shocked monazite chronometry: integrating microstructural and in situ isotopic age data for determining precise impact ages

Timmons M. Erickson[1] · Nicholas E. Timms[1] · Christopher L. Kirkland[1] · Eric Tohver[2] · Aaron J. Cavosie[1,3] · Mark A. Pearce[4] · Steven M. Reddy[1]

Received: 30 August 2016 / Accepted: 10 January 2017 / Published online: 16 February 2017

Abstract Monazite is a robust geochronometer and occurs in a wide range of rock types. Monazite also records shock deformation from meteorite impact but the effects of impact-related microstructures on the U–Th–Pb systematics remain poorly constrained. We have, therefore, analyzed shock-deformed monazite grains from the central uplift of the Vredefort impact structure, South Africa, and impact melt from the Araguainha impact structure, Brazil, using electron backscatter diffraction, electron microprobe elemental mapping, and secondary ion mass spectrometry (SIMS). Crystallographic orientation mapping of monazite grains from both impact structures reveals a similar combination of crystal-plastic deformation features, including shock twins, planar deformation bands and neoblasts. Shock twins were documented in up to four different orientations within individual monazite grains, occurring as compound and/or type one twins in (001), (100), $(10\bar{1})$, {110}, {212}, and type two (irrational) twin planes with rational shear directions in $[0\bar{1}\bar{1}]$ and $[\bar{1}\bar{1}0]$. SIMS U–Th–Pb analyses of the plastically deformed parent domains reveal discordant age arrays, where discordance scales with increasing plastic strain. The correlation between discordance and strain is likely a result of the formation of fast diffusion pathways during the shock event. Neoblasts in granular monazite domains are strain-free, having grown during the impact events via consumption of strained parent grains. Neoblastic monazite from the Inlandsee leucogranofels at Vredefort records a $^{207}Pb/^{206}Pb$ age of 2010 ± 15 Ma (2σ, $n = 9$), consistent with previous impact age estimates of 2020 Ma. Neoblastic monazite from Araguainha impact melt yield a Concordia age of 259 ± 5 Ma (2σ, $n = 7$), which is consistent with previous impact age estimates of 255 ± 3 Ma. Our results demonstrate that targeting discrete microstructural domains in shocked monazite, as identified through orientation mapping, for in situ U–Th–Pb analysis can date impact-related deformation. Monazite is, therefore, one of the few high-temperature geochronometers that can be used for accurate and precise dating of meteorite impacts.

Keywords Shock metamorphism · Monazite · Araguainha · Vredefort · U–Pb geochronology · EBSD

Communicated by Othmar Müntener.

Electronic supplementary material The online version of this article (doi:10.1007/s00410-017-1328-2) contains supplementary material, which is available to authorized users.

✉ Timmons M. Erickson
Timmons.Erickson@gmail.com

[1] TIGeR (The Institute of Geoscience Research), Department of Applied Geology, Curtin University, 1984, Perth, WA 6845, Australia

[2] School of Earth and Environment, University of Western Australia, Perth, WA 6009, Australia

[3] NASA Astrobiology Institute, Department of Geoscience, University of Wisconsin-Madison, Madison, WI 53706, USA

[4] CSIRO Mineral Resources, Australian Resources Research Centre, 26 Dick Perry Avenue, Kensington, WA 6151, Australia

Introduction

Impact cratering is one of the most ubiquitous processes in the solar system (French and Koeberl 2010). Because terrestrial impact craters form basins that are subject to erosion, burial and destruction by plate tectonic activity, the record of meteorite impacts on Earth is incomplete, limited to 190 confirmed structures (Earth Impact Database 2011).

The majority of confirmed impact craters on Earth have poor age constraints due to the lack of suitable geochronometers (Jourdan et al. 2009, 2012). As a consequence, fundamental questions regarding the connections between impact events and significant changes to both the lithosphere and biosphere remain unanswered. Shock deformation microstructures in minerals are one of a limited number of diagnostic criteria used to identify an impact event (French and Koeberl 2010). Crystal-plastic deformation caused by shock metamorphism has been shown to reset U–Th–Pb systems in some minerals to the time of impact (Moser et al. 2009, 2011; Cavosie et al. 2015a). It is, therefore, important to understand the effects of shock metamorphism on U–Th–Pb systematics to accurately date impact events (e.g. Moser et al. 2011).

Monazite, (La,Ce,Th)PO_4, is a common accessory phase that has been used as a tracer to study a variety of crustal processes due to the incorporation of U, Th, and other trace elements into its crystal structure (Catlos 2013). Even though shocked monazite has been reported from a few impact environments (e.g. Schärer and Deutsch 1990), recent advancements in electron backscatter diffraction (EBSD) mapping have permitted the systematic quantification of crystal-plastic deformation in monazite (e.g. Erickson et al. 2016a). However, the effects of specific impact-related deformation microstructures on the U–Th–Pb systematics in monazite have not been evaluated. In this study, we use EBSD to document shock microstructures in monazite from both the Vredefort Dome (South Africa) and Araguainha (Brazil) impact structures. Discrete domains were then targeted for secondary ion mass spectrometery (SIMS) analysis to understand what effects these features have on the U–Th–Pb ages of shocked monazite, and to identify specific microstructures that yield accurate impact ages.

Shock deformation microstructures

Meteorite impacts generate extremely high pressures (10 s of GPa and greater) in target rocks over instantaneous time periods (ms–s; Melosh 1989). The passage of the shock front through the target and impactor creates unique microstructural deformation, such as high-pressure phases, planar microstructures, and twins (French and Koeberl 2010). Minerals with unique impact-related deformation are commonly referred to as shocked minerals (Langenhorst and Deutsch 2012). The conditions required to develop shock deformation features vary with host mineral, and are best constrained for quartz. Quartz develops multiple sets of crystallographically controlled lamellae called planar deformation features (PDF) that form between 10 and 34 GPa. At higher pressures, quartz transforms to diaplectic SiO_2, which may revert to stishovite or coesite during release of the shock pressures (Stöffler and Langenhorst 1994). Of common accessory phases, zircon has the most well-constrained impact-related microstructures, which develop by 20 GPa (Leroux et al. 1999). Deformation twins are ubiquitous in shocked zircon, and have been observed in both static diamond anvil cell experiments at 20 GPa (Morozova 2015) and a variety of impact environments (e.g. Moser et al. 2011; Timms et al. 2012; Erickson et al. 2013a). At higher pressure, zircon transforms to the high-pressure polymorph reidite (Leroux et al. 1999; Wittmann et al. 2006; Reddy et al. 2015; Cavosie et al. 2015b; Erickson et al. 2017), which occurs at or above 30 GPa in shock experiments (Kusaba et al. 1985; Leroux et al. 1999). At more extreme shock conditions, zircon can develop granular texture (Bohor et al. 1993; Wittmann et al. 2006; Cavosie et al. 2015a, 2016; Timms et al. 2017). Granular zircon with systematic misorientations of 90°/<110> and 65°/<110> likely result from recrystallization of reidite and zircon {112} twins, respectively, and can contain evidence of partial dissociation to ZrO_2 that requires extreme temperature excursions due to the impact event (Cavosie et al. 2016; Timms et al. 2017).

Deformation microstructures in monazite

A range of deformation-related microstructures have been reported in monazite, including mechanical twinning, lattice strain, and recrystallization. Monazite deformation twins in (100), (001), {120} and {12$\bar{2}$} have been produced in indentation experiments at ambient temperature and pressure and imaged by transmission electron microscopy (TEM) (Hay and Marshall 2003). In tectonically deformed monazite, mechanical twins, crystal-plastic strain, and dynamically recrystallized neoblasts were identified by EBSD (Erickson et al. 2015). Crystal-plastic deformation, including low-angle (<10°) subgrain boundaries, was predominantly accomplished by slip systems which result in misorientations about <010> and <101>, and sets of deformation twins were found in (100), (001), and {12$\bar{2}$} (Erickson et al. 2015), which are the same twin orientations found in experimental studies (Hay and Marshall 2003). In the tectonically deformed monazite grains, strain-free neoblasts nucleated within high-strain domains and consumed the parent monazite by grain boundary migration (Erickson et al. 2015). Within the deformed monazite, the U–Th–Pb systematics were disturbed and variable age resetting was shown to correlate with plastic strain; the authors interpreted that Pb-loss was facilitated by formation of fast diffusion pathways during deformation (Erickson et al. 2015). Nucleation and growth of neoblastic monazite was driven by strain energy within the deformed lattice. Neoblasts excluded inherited Pb, and record Neoproterozoic U–Pb ages consistent with the age of regional

tectonometamorphism (Buick et al. 2010; Erickson et al. 2015).

Naturally shocked monazite with planar fractures was first reported from the ca. 39 Ma, 23 km diameter, Haughton impact structure, Canada (Schärer and Deutsch 1990). Shock-deformed monazite with planar microstructures and granular textures have since been described in bedrock from the Vredefort Dome, South Africa (Moser 1997; Hart et al. 1999; Flowers et al. 2003) and the Araguainha impact crater, Brazil (Tohver et al. 2012; Silva et al. 2016). Most prior studies documented microstructures using BSE images; however, lattice strain in the above examples has not been quantitatively characterized.

In addition to occurrences in bedrock, shocked monazite has also been identified in detrital populations derived from the Vredefort Dome (Cavosie et al. 2010, in press; Erickson et al. 2013b). Monazite grains containing planar features were found within the Vaal River and its tributaries, which cross-cut the Vredefort Dome (Cavosie et al. 2010), at sites up to 750 km downriver (Erickson et al. 2013b), and in Pleistocene fluvial terraces of the Vaal River (Cavosie et al. in press). Microstructural analysis of detrital shocked monazite by EBSD (Erickson et al. 2016a) identified a variety of deformation microstructures including sets of twins in up to 10 different orientations, planar deformation bands (PDBs) and neoblasts. Seven twin relationships were documented in the detrital shock monazite grains that have not been observed in tectonically deformed grains; these features have been attributed to shock deformation, and occur along with the twin types reported in tectonically deformed monazite (100), (001), and $\{12\bar{2}\}$ (Erickson et al. 2016a). Critically, the detrital shocked monazite grains contain zircon inclusions exhibiting {112} twins that require minimum shock pressures of 20 GPa, thus providing an empirical constraint on the shock features in the host monazite grains. Erickson et al. (2016a) interpreted that the seven previously unreported twin orientations, including $(10\bar{1})$, $\{\bar{1}10\}$, $(10\bar{2})$, $\{212\}$, $\{\bar{1}\bar{2}0\}$, and two irrational planes containing shear directions (η_1) in $[01\bar{1}]$ and $[\bar{1}\bar{1}0]$ represent bona fide shock microstructures.

Several studies have addressed the aspects of experimental shock deformation on microstructural and isotopic systematics of monazite. An experimental study by Deutsch and Schärer (1990) tested the effects of shock metamorphism on the U–Pb systematics by subjecting a monazite crystal to 59 GPa and temperatures >1200 °C followed by rapid cooling. While the experiment yielded monazite with significantly lower birefringence, intense mosaicism and sub-parallel fractures (Deutsch and Schärer 1990; their Fig. 3b), the authors found no significant disturbance to the U–Pb isotopic system. It has been noted that shock experiments may not represent the full range of shock deformation features found in nature (Deutsch and Schärer 1990; Niihara et al. 2012), given the timescales of experiments are orders-of-magnitude shorter than natural impact events. Other studies have analyzed the effects of the high-pressure shock wave caused by plasma expansion during femtosecond laser ablation analysis of monazite (Seydoux-Guillaume et al. 2010; D'Abzac et al. 2012). Microstructural features observed within the region directly adjacent to the laser ablation pit include deformation twinning, crystal-plasticity, mosaicism and the formation of micron-scale granules (Seydoux-Guillaume et al. 2010; D'Abzac et al. 2012).

Naturally shocked monazite grains with planar microstructures from Vredefort bedrock (Flowers et al. 2003) and detritus (Erickson et al. 2013b) were found to record pre-impact ages when analyzed by thermal ionization mass spectrometry (TIMS) and SIMS, respectively. However, monazite that has recrystallized during shocked metamorphism and yields impact ages has been reported at both the Vredefort Dome (Moser 1997) and Araguainha structures (Tohver et al. 2012). Because deformation can variably reset the U–Pb systematics in monazite (Wawrzenitz et al. 2012; Erickson et al. 2015, 2016b), shock-deformed monazite may be a valuable impact chronometer. In this study, we analyzed monazite and zircon from the Inlandsee leucogranofels located in the central uplift of the Vredefort Dome and in impact melt from the Araguinha impact structure. The aim of this study is three-fold: first, to systematically characterize shock microstructures in monazite from these impact craters to compare shocked monazite from different impact environments ; second, constrain the shock conditions experienced by monazite through analysis of deformation microstructures in zircon from the same samples; third, to quantify the effects of shock deformation on U–Th–Pb ages in monazite with well-characterized microstructures from impact craters where the impact age has been independently constrained to rigorously evaluate the application of shocked monazite as an impact chronometer.

Geologic background and samples

Vredefort impact structure, South Africa

The Vredefort impact structure is a ca. 2020 Ma deeply eroded crater located within the Kaapvaal Craton in South Africa (Kamo et al. 1996; Gibson et al. 1997; Moser 1997). The Vredefort Dome is the ~90-km-diameter erosional remains of the central uplift of the complex crater. The central uplift contains a complex internal structure consisting of a 40-km-diameter inner core, comprising the granulite facies Inlandsee leucogranofels (ILG) and the amphibolite facies Outer Granite Gneiss, and an outer collar which consists of a ~25-km-thick ring of over-turned Archean and Paleoproterozoic metasedimentary and metavolcanic rocks

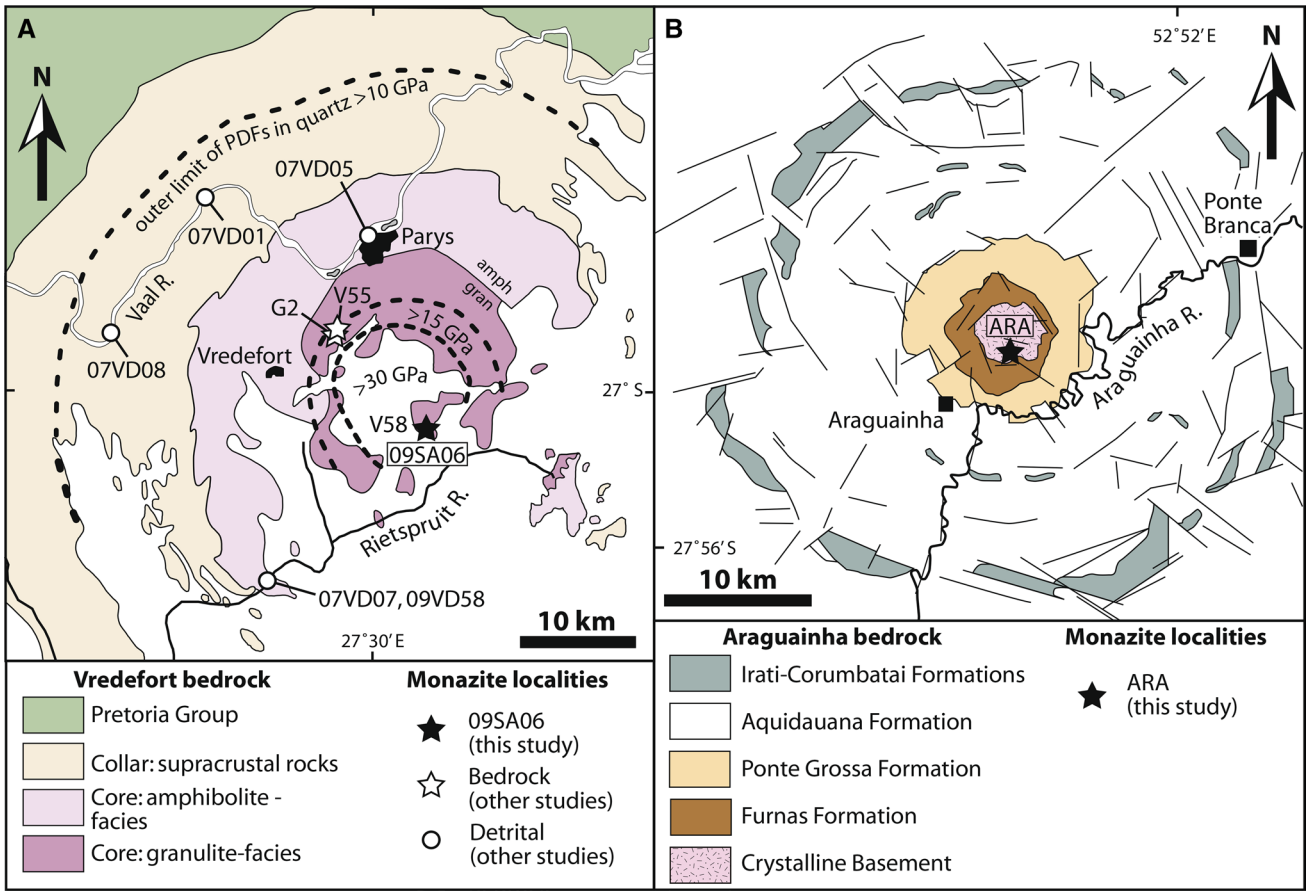

Fig. 1 Bedrock maps of the Vredefort Dome and Araguainha impact structures with sample locations. **a** Simplified bedrock map of the Vredefort Dome impact structure, South Africa, modified from Bischoff et al. (1999). The location of sample 09SA06 (this study) is the same as V58 (Moser 1997). Other shocked monazite bedrock samples; G2 (Hart et al. 1999) and V55 (Flowers et al. 2003), and detrital samples; 07VD0 (1, 5, 7 & 8), 09VD58 (Cavosie et al. 2010; Erickson et al. 2013b; 2016a, b) are also marked. Shock pressure isobars are taken from Gibson and Reimold (2005). **b** Simplified bedrock map of the Araguainha impact structure, Brazil, modified from Lana et al. (2007) with the location of sample ARA (this study), impact melt collected from within the central uplift

(Fig. 1a; Bischoff et al. 1999). The outer ring creates a topographic high around the weathered granitiods and gneisses, from which the upper 8–11 km have been removed (Gibson et al. 1998). Modeling of mineral indicators of impact pressures within the Vredefort Dome and structural studies of the surrounding Witwatersrand basin suggests that the transient crater was between 200 and 300 km wide (Ivanov 2005) and contained the entire Witwatersrand basin. The Vredefort Dome experienced post-impact, low-grade, metamorphism associated with emplacement of mafic intrusions at ca. 1000 Ma (Reimold et al. 2000), which may have resulted in Pb-loss within some zircon grains at this time (Moser et al. 2011).

The core of the Vredefort Dome comprises 3420–3000 Ma Archean granitoids, charnockitic gneiss, and supracrustal rocks metamorphosed at high regional grades in the Archean (Hart et al. 1999; Moser et al. 2001; Armstrong et al. 2006) that subsequently experienced pyroxene-hornfels metamorphism during the impact, where temperatures locally reached as high as 1300 °C (Gibson 2002). Three occurrences of shocked monazite have been reported from Vredefort bedrock (Fig. 1a; Moser 1997; Hart et al. 1999; Flowers et al. 2003). Shocked monazite that record pre-impact ages with partial Pb-loss were reported by Hart et al. (1999) from a granulite-facies garnetiferous paragneiss, near the center of the Vredefort Dome. Shocked monazite with cross-cutting planar microstructures within gneissic quartz monzonite near the granulite–amphibolite transition within the Vredefort Dome was dated by ID-TIMS by Flowers et al. (2003). The U–Th–Pb analysis documented partial Pb-loss, defining an age array from 3180 to 2260 Ma. The authors interpreted upper intercepts to represent regional metamorphism associated with intrusions between 3130 and 3080 Ma (Flowers et al. 2003).

Monazite with granular texture from the ILG, located at the center of the Vrededort Dome, record complete isotopic age resetting (Moser 1997). The ILG (Stepto 1990) is composed of a sequence of felsic high-grade metamorphosed, migmatitic Archean TTG, enderbite and charnockite (Flowers et al. 2003), all thermally recrystallized by the shock event (Gibson and Reimold 2005). Two granular monazite grains dated by ID-TIMS (Moser 1997) yielded $^{207}Pb/^{206}Pb$ ages of 2090 ± 4 (2σ), and 2016 ± 7 (2σ), the latter of which is within error of impact-generated zircon at Vredefort (Kamo et al. 1996; Gibson et al. 1997; Moser 1997). Zircon from the same ILG sample yielded a discordant U–Pb array, with an upper intercept of 3290 Ma and lower intercept of ca. 2020 Ma (Moser 1997). Moser et al. (2011) analyzed shocked zircon from the ILG using EBSD. The authors identified low-angle boundaries, shock twins and sub-planar fractures. U–Pb SIMS analysis of the ILG zircon displayed a discordant array, from which three of four analyses spread between 3471 ± 61 Ma and 2020 Ma (Moser et al. 2011). A sample of ILG foliated felsic gneiss, 09SA06 (Fig. 1a), was selected for analysis by EBSD and SIMS because monazite grains reported from the ILG show significant recrystallization textures (Moser 1997), the zircon grains preserve shock twinning and plastic deformation (Moser et al. 2011), and variable resetting of the U–Th–Pb systems was detected between the two phases.

Araguainha impact structure, Brazil

The ca. 255 Ma Araguainha impact structure is a ~40-km-diameter complex crater located within the Paraná Basin of central Brazil (Tohver et al. 2012). The impact punctured 1500–1800 m thick Permian to Devonian stratigraphy of the Paraná Basin, exposing Cambrian granitic basement within the ~5-km-diameter central uplift (Fig. 1b; Lana et al. 2007, 2008; Tohver et al. 2012). The Araguainha granite is a pink, coarse-grained monzo-syenogranite, with a crystallization age of 510 ± 12 Ma (Tohver et al. 2012). The granite is cross-cut by an impact melt-bearing, polymictic breccia, or suevite (Engelhardt et al. 1992), dominantly derived from the local granite (Machado et al. 2009; Tohver et al. 2012).

Shock-deformed monazite grains have been identified within shocked Araguainha granite, partially melted granite, suevite, and within melt sheet/veins in the central uplift (Tohver et al. 2012; Silva et al. 2016). Monazite grains from shocked granite show cross-cutting, double-walled, planar features (Silva et al. 2016), that appear consistent with shock twins reported elsewhere (cf. Erickson et al. 2016a). In partially melted granite, monazite grains show an annealed texture, consistent with dynamic recrystallization (Silva et al. 2016). Within Araguainha impact melt, Silva et al. (2016) identified multiple textures within the monazite grains, including planar features, annealed polycrystalline aggregates, and a distinctive cataclastic microstructure.

Two types of shock features were identified within monazite from the impact melt rock of Tohver et al. (2012), including planar fractures and 'granular aggregates'. Planar fractures display trails of inclusions cross-cutting the monazite in polished section, while aggregates of 'neocrystallized' monazite granules display curved boundaries and form triple junctions (Tohver et al. 2012; their Fig. 6). Shocked monazite grains were dated by Tohver et al. (2012) and show a bimodal age distribution, with ages spread between ca. 500 and 250 Ma, which the authors interpreted as representing both inherited deformed monazite and impact-generated recrystallized monazite. Domains containing planar microstructure record the oldest ages, which range from ca. 498 to ca. 350 Ma. The population of monazite made up of aggregates of neocrystalline granules records an U–Th–Pb age of 255 ± 3 Ma, which the authors interpreted as the age of the Araguainha impact (Tohver et al. 2012). Due to the complex microstructures exhibited by the shocked monazite from Araguainha impact melt (AIM) sample of Tohver et al. (2012) and their bimodal age distribution, we selected this sample for EBSD and further SIMS analysis.

Methods

Monazite and zircon were separated from ILG sample 09SA06 (27°2.870′S, 27°29.603′E) and from AIM sample ARA (16°49.329′S, 53°0.150′W) of Tohver et al. (2012). Monazite and zircon were analyzed by EBSD using previously established approaches (Reddy et al. 2007; Erickson et al. 2015). Scanning electron microscopy, including EBSD analysis, was undertaken with a Tescan Mira3 Field emission gun scanning electron microscope within the John de Laeter Centre (JDLC) at Curtin University. For further details on the methodologies see Appendix 1. Additional EBSD maps for zircon and monazite from 09SA06 and ARA can be found in appendices 2–5, respectively. U–Th–Pb SIMS analysis of shocked monazite grains was undertaken with a SHRIMP II housed within the JDLC after the methods of (Fletcher et al. 2010); see appendix 1 for more details. The cumulative crystal-plastic misorientation within each SIMS analytical domain was calculated from the equivalent region of the EBSD maps (e.g. Figs. 2c, 4c) as the grain orientation spread (GOS and GOS avg.); for further details on this calculation see Appendix 1. Element maps of monazite grains were acquired using a Cameca SXFive electron probe microanalyzer (EPMA) at Adelaide Microscopy at the University of Adelaide (see Appendix 1).

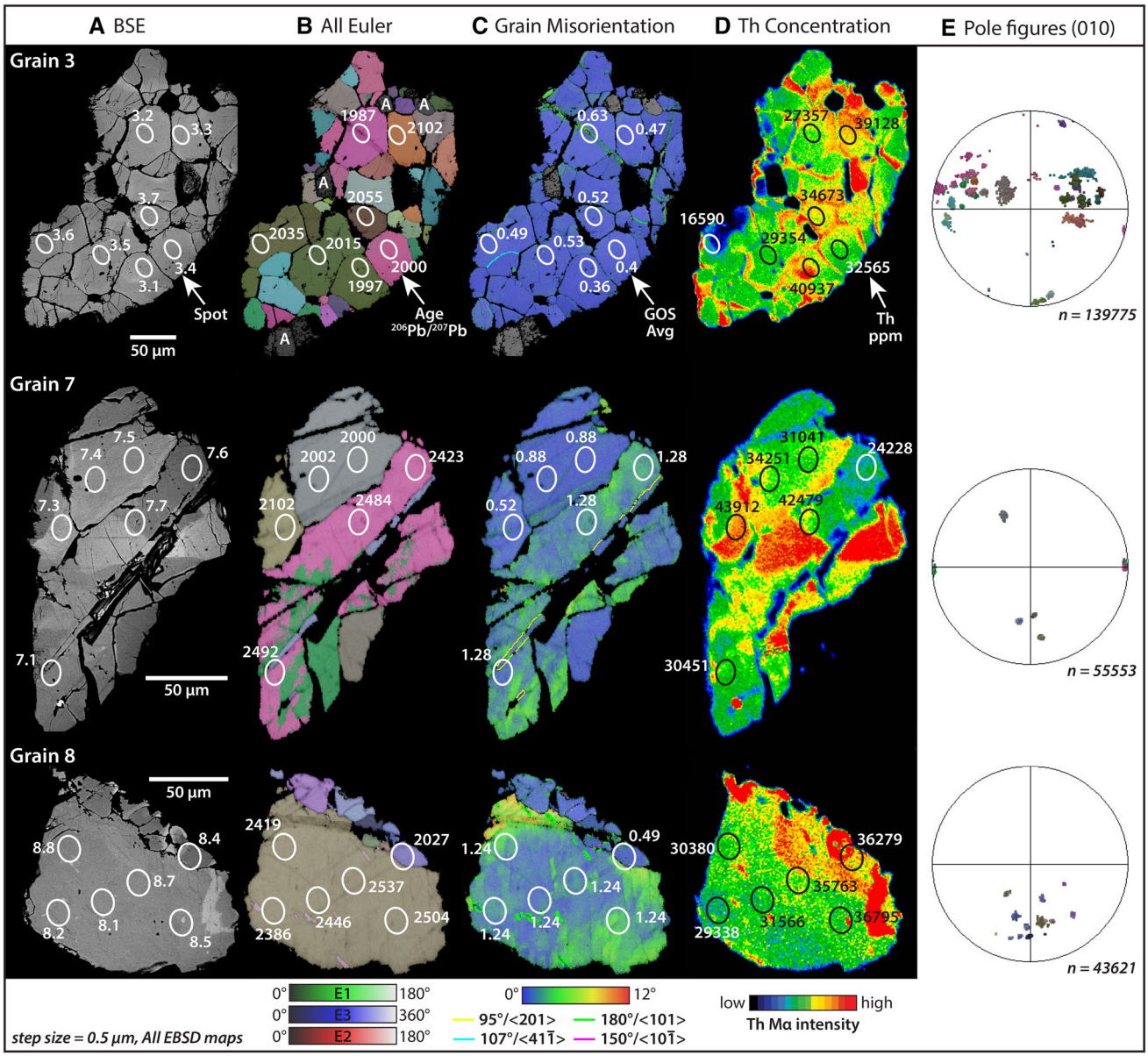

Fig. 2 Shock-deformed monazite from sample 09SA06 from the Inlandsee leucogranofels (ILG). **a** Backscattered electron (BSE) atomic number contrast photomicrographs with the location of each SIMS U–Th–Pb analytical spot marked on the grains. **b** Electron backscatter diffraction (EBSD) crystallographic orientation map, colored with an all Euler scheme, SIMS $^{207}Pb/^{206}Pb$ age measurements are marked for each spot. Apatite inclusions in grain 3 are marked *A*. **c** EBSD grain misorientation map, which helps visualize the substructure of the grains by plotting the misorientation angle of each pixel from the mean grain orientation. Each SIMS spot is labeled with the calculated average grain orientation spread (GOS avg.) for each subdomain, see text for details of the calculation. Grain boundaries are defined by misorientation threshold of >10°. *Blue* domains are low strain, while *warm colors* represent higher degrees of misorientation. Additionally, boundaries between adjacent pixels are color-coded if they matched a specific misorientation axis and angle pair, within 5°, such as a known twin misorientation. **d** Electron microprobe analyzer (EPMA) maps of Th Mα intensity, with measured Th concentrations (in ppm) for each SIMS spot. **e** Pole figures of monazite (010) colored with an all Euler scheme. Grain 3 is a shocked monazite which has completely converted to neoblasts by dynamic recrystallization. Monazite grains 7 and 8 contain both domains dominated by plastic strain and deformation twins and domains with low-strain neoblasts

Results

Orientation maps of eight monazite and four zircon grains from sample 09SA06 from the Vredefort ILG were made using EBSD. An additional 11 monazite and three zircon grains were analyzed from sample ARA from the Araguainha impact melt. Monazite and zircon microstructures are summarized below. Also, U–Th–Pb analyses

targeting specific microstructural domains for monazite grains from both samples are reported in Tables 1 and 2.

Vredefort ILG-monazite microstructures

Monazite grains from the ILG contain multiple types of microstructure, including crystal-plastic strain, deformation twinning and randomly oriented, low-strain subdomains. The grains are variably complex, from being dominated by crystal-plastic strain with a combination of low-angle boundaries and deformation twins (e.g. Grain 8, Fig. 2), to dominated by randomly oriented subdomains (e.g. Grain 3, Fig. 2), or a combination of both microstructural types (e.g. Grain 7, Fig. 2). Four monazite grains contain deformation twins, which occur in up to two orientations per grain, with the following minimum misorientation relationships (as angle/axis pairs) from the host grain; 180°/<101>, 95°/<201> and 150°/< $10\bar{1}$ >, which are consistent with twins in $(10\bar{1})$, $\{1\bar{2}\bar{2}\}$ and {212}, respectively (Erickson et al. 2016a). Grain 3 is composed entirely of strain-free subdomains, which range between 68.6 and 1.7 μm diameter (mean = 17.5 μm). Elemental maps for Th reveal complex zonation textures; within the high-strain domains, the grains preserve either concentric (grain 8) or patchy zonation (grain 7), while some of the strain-free subdomains preserve sector zoning patterns (grain 3, Fig. 2d).

The eight ILG monazite grains contain a variety of intergrowths and/or inclusions, including both zircon (2 of 8) and apatite (5 of 8) grains. The apatite inclusions occur within both crystal-plastically strained domains (e.g. grain 1, appendix 2) and within low-strain subdomains (e.g. grain 3, Fig. 2) of the monazite grains, and, therefore, predate shock deformation. Two monazite grains also contain zircon inclusions (grains 1, 4, appendix 2), which record minor degrees of crystal-plastic strain, but no features diagnostic of shock deformation (cf., Erickson et al. 2016a).

Vredefort ILG-zircon microstructures

Cathodoluminescence (CL) images of zircon from the ILG reveal dark, concentrically zoned cores, and bright sector zoned rims (Fig. 3a). Lamellae that are bright in CL also cross-cut growth zoning, which is especially evident in the CL dark cores. All four zircon grains mapped by EBSD contain twin lamellae that are misoriented 65°/<110> with the host grain, and align with the bright CL lamellae (appendix 3). However, the localized bright CL sections of some lamellae are in the crystallographic orientation of the parent grain, rather than preserving a twin orientation (Fig. 3a, c).

Araguainha impact melt-monazite microstructures

Shock-deformed monazite grains within the AIM contain similar microstructures to the ILG monazite, including crystal-plastic strain, deformation twinning and strain-free domains. Of eleven grains analyzed by EBSD, all contain crystal-plastically strained domains with sub-planar low-angle boundaries (e.g. grains 10, 11, Fig. 4). The grains each contain between 1 and 4 sets of deformation twins with the following minimum misorientation relationships; 180°/<100>, 180°/<001>, 180°/<101>, 94°/<001>, 150°/< $10\bar{1}$ >, 85°/<401> and 91°/<104>. The twins are consistent with known monazite twin orientations observed at the Vredefort Dome; compound twin planes in (001), (100), $(10\bar{1})$, type 1 (rational) twin planes in {110}, {212} and type two (irrational) twin planes with rational shear directions (η1) in $[0\bar{1}\bar{1}]$ and $[\bar{1}\bar{1}0]$, respectively (Erickson et al. 2016a). Many shock twins are discontinuous, and have irregular, non-planar interfaces but fall along linear traces (Fig. 5b). Ten of the eleven monazite grains also contain strain-free domains, which are randomly oriented relative to the strained parent grains, and range in diameter between 24.5 and 1.0 μm, with a mean diameter of 8.0 μm (Figs. 4, 5). Elemental maps of Th reveal concentric or sector zonation patterns, which are moderately overprinted by a patchy texture (Fig. 4d). In grain 10, the strain-free, randomly oriented domains, correspond with the zone of highest Th concentrations in the grain; however, other grains do not show this pattern. Only one of the analyzed shocked monazite grains from Araguainha contains a zircon inclusion (~10 μm), which preserves a polycrystalline microstructure (granular texture) similar to that described in Cavosie et al. (2016).

Araguainha impact melt-zircon microstructures

Three shocked zircon grains from the AIM contain a variety of both crystal-plastic and recrystallization textures. The zircon grains contain {100} PDBs, a {112} twin lamella in one grain, and granular texture (appendix 5). The most complex zircon analyzed (Fig. 6) contains a crystal-plastically strained parent grain and misoriented subdomains. The subdomains include areas that are systematically misoriented from the parent grain with 65°/<110> or 90°/<110> relationships, and also neoblasts that are randomly oriented (Fig. 6b–e). The neoblasts range between 1.0 and 6.9 μm in diameter (mean equivalent circle diameter = 1.8 μm).

Monazite in situ U–Th–Pb geochronology

A total of 19 SIMS analytical spots were collected from three monazite grains from the ILG sample 09SA06; seven

Table 1 SIMS U–Th–Pb analyses for shocked monazite from the Vredefot Inlandsee leucogranofels (09SA06)

Analytical spot	Domain	U (ppm)	Th (ppm)	Th/U	$f^{206}Pb$ %	$^{208}Pb^*/^{232}Th$	$^{207}Pb^*/^{235}U$	$^{206}Pb^*/^{238}U$	$^{207}Pb^*/^{206}Pb$	$^{208}Pb^*/^{232}Th$ Age (Ma)	$^{206}Pb^*/^{238}U$ Age (Ma)	$^{207}Pb^*/^{206}Pb^*$ Age (Ma)	% disc. [a]	% disc. [b]	Grain orientation spread (avg)
09SA06-3.1	Neoblast	584	40,937	70.13	−0.08	0.0991 ± 0.0015	5.972 ± 0.116	2.8355 ± 0.0061	0.12280 ± 0.00109	1972 ± 17	1947 ± 28	1997 ± 16	2.6	1.3	0.4
09SA06-3.2	Neoblast	484	27,375	56.51	−0.04	0.1005 ± 0.0015	5.822 ± 0.133	2.8909 ± 0.0060	0.12207 ± 0.00180	1950 ± 20	1915 ± 28	1987 ± 26	3.7	1.8	0.63
09SA06-3.3	Neoblast	168	39,128	233.14	0.81	0.0968 ± 0.0014	6.234 ± 0.193	2.8824 ± 0.0078	0.13032 ± 0.00276	2009 ± 27	1920 ± 37	2102 ± 37	9.5	4.6	0.47
09SA06-3.4	Neoblast	527	32,564	61.78	−0.10	0.0969 ± 0.0014	5.929 ± 0.125	2.8596 ± 0.0062	0.12297 ± 0.00143	1966 ± 18	1933 ± 29	2000 ± 21	3.4	1.7	0.36
09SA06-3.5	Neoblast	551	29,345	53.27	1.10	0.0979 ± 0.0015	5.969 ± 0.151	2.8648 ± 0.0061	0.12402 ± 0.00225	1971 ± 22	1930 ± 29	2015 ± 32	4.4	2.1	0.53
09SA06-3.6	Neoblast	358	16,590	46.38	0.95	0.1014 ± 0.0015	6.074 ± 0.136	2.8483 ± 0.0066	0.12547 ± 0.00154	1986 ± 19	1940 ± 31	2035 ± 22	4.9	2.4	0.49
09SA06-3.7	Neoblast	234	34,673	148.49	0.72	0.0990 ± 0.0015	6.069 ± 0.151	2.8821 ± 0.0071	0.12685 ± 0.00178	1986 ± 21	1920 ± 34	2055 ± 25	7.0	3.4	0.52
09SA06-7.1	Host	686	30,451	44.41	2.91	0.0986 ± 0.0016	8.736 ± 0.187	2.5806 ± 0.0068	0.16350 ± 0.00201	2311 ± 19	2111 ± 31	2492 ± 21	18.0	9.5	1.28
09SA06-7.3	Neoblast	202	43,912	217.69	0.42	0.0999 ± 0.0014	6.298 ± 0.128	2.8530 ± 0.0062	0.13033 ± 0.00132	2018 ± 18	1937 ± 29	2102 ± 18	8.5	4.2	0.52
09SA06-7.4	Neoblast	176	34,251	194.30	−0.88	0.0977 ± 0.0015	5.643 ± 0.126	3.0074 ± 0.0059	0.12309 ± 0.00165	1923 ± 19	1851 ± 28	2002 ± 24	8.2	3.9	0.88
09SA06-7.5	Neoblast	172	31,041	180.88	−0.87	0.0975 ± 0.0014	5.863 ± 0.135	2.8925 ± 0.0061	0.12299 ± 0.00181	1956 ± 20	1914 ± 29	2000 ± 26	4.5	2.2	0.88
09SA06-7.6	Host	633	24,228	38.26	−0.04	0.1075 ± 0.0015	8.548 ± 0.183	2.5320 ± 0.0070	0.15696 ± 0.00190	2291 ± 19	2146 ± 32	2423 ± 20	12.9	6.8	1.28
09SA06-7.7	Host	754	42,479	56.34	0.13	0.1134 ± 0.0016	9.231 ± 0.179	2.4296 ± 0.0072	0.16266 ± 0.00135	2361 ± 18	2222 ± 33	2484 ± 14	11.8	6.3	1.28
09SA06-8.1	Host	1076	31,566	29.32	−0.08	0.1042 ± 0.0016	8.708 ± 0.174	2.5183 ± 0.0067	0.15905 ± 0.00171	2308 ± 18	2156 ± 30	2446 ± 18	13.5	7.1	1.24
09SA06-8.2	Host	1109	29,338	26.44	−0.09	0.1002 ± 0.0014	8.311 ± 0.145	2.5470 ± 0.0061	0.15352 ± 0.00121	2265 ± 16	2135 ± 28	2386 ± 13	11.7	6.1	1.24
09SA06-8.4	Neoblast	418	36,279	86.77	3.58	0.0910 ± 0.0013	5.942 ± 0.196	2.8973 ± 0.0058	0.12486 ± 0.00354	1967 ± 28	1911 ± 28	2027 ± 50	6.0	2.9	0.49
09SA06-8.5	Host	1172	36,795	31.39	−0.06	0.1020 ± 0.0015	9.246 ± 0.170	2.4560 ± 0.0064	0.16469 ± 0.00158	2363 ± 17	2202 ± 29	2504 ± 16	13.7	7.3	1.24
09SA06-8.7	Host	791	35,763	45.24	−0.14	0.1047 ± 0.0015	9.895 ± 0.175	2.3400 ± 0.0067	0.16794 ± 0.00134	2425 ± 16	2294 ± 30	2537 ± 13	10.6	5.7	1.24
09SA06-8.8	Host	950	30,380	31.96	−0.12	0.1009 ± 0.0015	8.436 ± 0.152	2.5596 ± 0.0061	0.15660 ± 0.00140	2279 ± 16	2126 ± 28	2419 ± 15	13.8	7.2	1.24

$f^{206}Pb$ is the proportion of ^{206}Pb calculated to be common Pb on the basis of measured $^{204}Pb/^{206}Pb$ and modelled common Pb composition (Stacey and Kramers 1975) at the approximate sample age

Listed uncertainties are 1σ

disc. discordance, *uncalc*. uncalculated

‡Grain orientation spread (avg) calculated from EBSD data, see methods for further details

*All listed Pb isotope data are corrected for common Pb, based on measured $^{204}Pb/^{206}Pb$

% Discordance[a] calculated as $[(^{207}Pb/^{206}Pb)-(^{206}Pb/^{238}U)]/(^{206}Pb/^{238}U)\times 100$

% Discordance[b] calculated as $[(^{208}Pb/^{232}Th)-(^{206}Pb/^{238}U)]/(^{206}Pb/^{238}U)\times 100$

Table 2 SIMS U–Th–Pb analyses for shocked monazite from the Araguainha impact melt (AIM)

Analytical spot	Domain	U (ppm)	Th (ppm)	Th/U	$f^{206}Pb$ %	$^{208}Pb^*/^{232}Th$	$^{207}Pb^*/^{235}U$	$^{206}Pb^*/^{238}U$	$^{207}Pb^*/^{206}Pb$	$^{208}Pb^*/^{232}Th$ Age (Ma)	$^{206}Pb^*/^{238}U$ Age (Ma)	$^{207}Pb^*/^{206}Pb^*$ Age (Ma)	% disc. [a]	% disc. [b]	Grain orientation spread[‡]
ARA-10.1	Neoblast	335	13,163	39.3	9.53	0.01334 ± 0.0001	0.24458 ± 0.043228	0.0391 ± 0.4902	0.04552 ± 0.00820	268 ± 3	247 ± 5	−28 ± 387	−111.3	8.3	0.15
ARA-10.2	Neoblast	225	16,339	72.7	9.18	0.01309 ± 0.0001	0.35744 ± 0.039279	0.0390 ± 0.4507	0.06667 ± 0.00791	263 ± 2	247 ± 4	828 ± 230	235.2	6.5	Uncalc
ARA-10.3	Host	1285	21,858	17.0	5.63	0.01920 ± 0.0002	0.48867 ± 0.085749	0.0653 ± 0.2300	0.05449 ± 0.00944	384 ± 4	408 ± 6	391 ± 348	−4.0	−5.7	1.76
ARA-10.4	Host	375	18,055	48.1	3.18	0.01863 ± 0.0002	0.43894 ± 0.027374	0.0591 ± 0.2542	0.05410 ± 0.00351	373 ± 4	370 ± 5	375 ± 140	1.4	0.9	2.32
ARA-11.1	Host	1161	26,239	22.6	0.32	0.02144 ± 0.0002	0.55769 ± 0.010637	0.0725 ± 0.2937	0.05602 ± 0.00064	429 ± 4	451 ± 9	453 ± 25	0.4	−5.0	1.15
ARA-11.2	Neoblast	627	26,658	42.5	4.07	0.01320 ± 0.0001	0.30598 ± 0.027238	0.0416 ± 0.3531	0.05359 ± 0.00510	265 ± 2	263 ± 4	354 ± 202	34.8	1.0	0.15
ARA-11.3	Host	704	25,034	35.6	1.64	0.02033 ± 0.0002	0.50929 ± 0.016449	0.0709 ± 0.1911	0.05232 ± 0.00201	407 ± 4	441 ± 6	299 ± 85	-32.2	−7.9	1.12
ARA-11.4	Neoblast	621	35,834	57.7	2.21	0.01271 ± 0.0001	0.27875 ± 0.011426	0.0420 ± 0.3273	0.04834 ± 0.00250	255 ± 2	265 ± 4	116 ± 118	-56.2	−3.7	0.19
ARA-11.5	Neoblast	559	28,645	51.3	1.79	0.01304 ± 0.0001	0.30526 ± 0.010204	0.0411 ± 0.3329	0.05411 ± 0.00239	262 ± 2	260 ± 3	376 ± 97	44.7	0.9	0.18
ARA-11.6	Host	285	13,909	48.7	5.85	0.01757 ± 0.0002	0.43476 ± 0.033228	0.0529 ± 0.2906	0.05990 ± 0.00500	352 ± 3	332 ± 5	600 ± 171	80.7	6.0	1.75
ARA-11.7	Neoblast	474	26,602	56.1	3.21	0.01264 ± 0.0001	0.33082 ± 0.015563	0.0407 ± 0.3472	0.05917 ± 0.00346	254 ± 2	257 ± 4	573 ± 122	122.9	−1.3	0.3
ARA-11.8	Host	245	11,160	45.6	10.96	0.01626 ± 0.0002	0.23739 ± 0.048583	0.0440 ± 0.5562	0.03929 ± 0.00845	326 ± 3	278 ± 7	−397 ± 484	−243.2	17.5	1.46
ARA-11.9	Neoblast	498	25,496	51.2	1.62	0.01260 ± 0.0001	0.29882 ± 0.010357	0.0420 ± 0.3947	0.05179 ± 0.00242	253 ± 2	265 ± 4	276 ± 103	4.1	−4.6	Uncalc
ARA-11.10	Host	611	25,999	42.5	0.49	0.02054 ± 0.0002	0.58502 ± 0.009420	0.0752 ± 0.1801	0.05666 ± 0.00104	411 ± 4	467 ± 6	479 ± 40	2.4	−12.1	1.25

$f^{206}Pb$ is the proportion of ^{206}Pb calculated to be common Pb on the basis of measured $^{204}Pb/^{206}Pb$ and modelled common Pb composition (Stacey and Kramers 1975) at the approximate sample age

Listed uncertainties are 1σ

disc. discordance, *uncalc*. uncalculated

[‡]Grain orientation spread calculated from EBSD data, see methods for further details

*All listed Pb isotope data are corrected for common Pb, based on measured $^{204}Pb/^{206}Pb$

% Discordance[a] calculated as $[(^{207}Pb/^{206}Pb)-(^{206}Pb/^{238}U)]/(^{206}Pb/^{238}U)\times 100$

% Discordance[b] calculated as $[(^{208}Pb/^{232}Th)-(^{206}Pb/^{238}U)]/(^{206}Pb/^{238}U)\times 100$

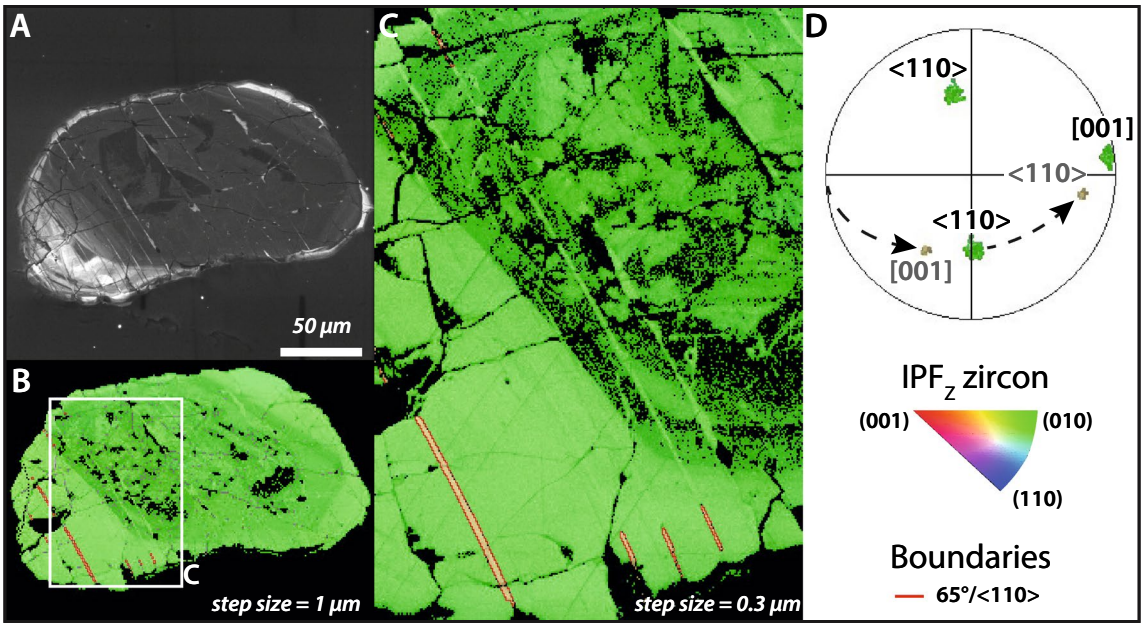

Fig. 3 Typical shocked zircon from ILG sample 09SA06. **a** Cathodoluminesce (CL) image of shocked zircon exhibiting a dark concentrically zoned core, with a brighter sector zoned rim. **b** EBSD orientation map of the zircon with an inverse pole figure (IPF$_z$) color scheme and a special boundary (65°/<110>) color for {112} shock twins. IPF colors correspond to crystallographic direction parallel to the normal to the map acquisition surface (*z*). **c** IPF and special boundary map of an area of interest of the zircon. The {112} lamellae cross-cutting the CL-dark core have annealed to the orientation of the host grain and correspond to bright CL lamellae. **d** Pole figure of data from map B, also with an IPF color scheme, highlighting the <110> misorientation axis of the shock twins

analyses from grain 3, six from grain 7 and six from grain 8. Eight analyses were obtained from crystal-plastically strained domains in grains 7 and 8, while eleven were acquired from low-strain subdomains (Grain orientation spread, GOS Avg., <0.9°) in all three grains (Fig. 2b). Apparent ages from ILG monazite show a bimodal age distribution (Fig. 7a). Analytical spots from the strained host are variably discordant (>10% between $^{206}Pb/^{207}Pb$ and $^{206}Pb/^{238}U$), with apparent $^{207}Pb/^{206}Pb$ ages between 2537 ± 26 and 2386 ± 26 Ma (2σ). Spots from the low-strain, randomly oriented subdomains show a tight cluster around concordia and are all <9% discordant, with $^{207}Pb/^{206}Pb$ ages ranging between 2102 and 1987 Ma (Fig. 7b). The analyses show a relationship between U–Th discordance and common Pb as estimated based on measured ^{204}Pb (Fig. 7b). Nevertheless, the nine most concordant analyses, (all <7.5% discordant) yield a weighted mean $^{207}Pb/^{206}Pb$ date of 2010 ± 15 (2σ, n = 9, MSWD = 0.84).

A total of 14 SIMS analytical spots were collected from two monazite grains from the Araguainha impact melt rock, ARA. Four spots were collected from grain 10 and ten spots from grain 11. Of the fourteen analytical spots, seven were acquired from crystal-plastically strained domains and seven were acquired from strain-free (grain orientation spread, GOS, <0.3°) subdomains (Fig. 8a, b). The data define a bimodal age distribution along concordia. Plastically strained domains have apparent $^{206}Pb/^{238}U$ ages ranging from 467 ± 12 to 278 ± 14 Ma, with the three oldest ages originating from the least strained portions of the parent grains (Fig. 8). Seven analyses from strain-free subdomains are clustered on concordia (<8% discordance between $^{208}Pb/^{232}Th$ and $^{206}Pb/^{238}U$) and yield $^{206}Pb/^{238}U$ ages between 265 and 247 Ma (Fig. 8). Analyses from strain-free subdomains yield a concordia age of 259 ± 5 Ma (2σ, n = 7, MSWD = 1.3). However, if the analyses from grain 11, which contains less common Pb and has better agreement between the U–Th systematics than those from grain 10, are solely considered, they yield a concordia age of 262 ± 3 (2σ, n = 5, MSWD = 0.88).

Discussion

Impact-related microstructures in monazite: twinning, PDBs, neoblasts

In both samples, monazite grains contain a combination of domains which are crystal-plastically strained, and domains that are randomly oriented and strain-free. The crystal-plastically strained domains preserve a combination of cumulative strain across the grain accommodated by low-angle grain boundaries, consistent with dislocation creep.

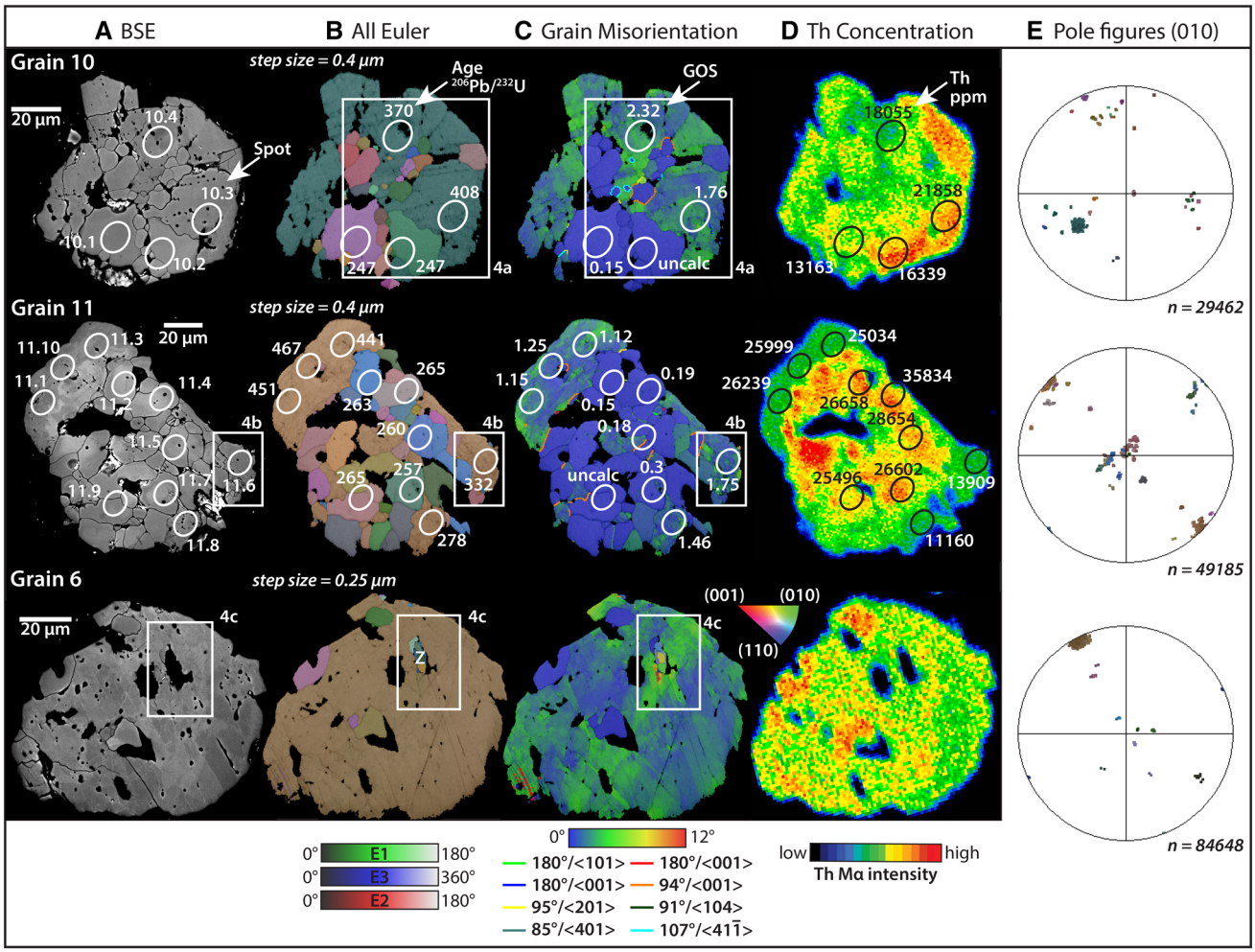

Fig. 4 Shock-deformed monazite from sample ARA from the Araguainha melt rock. **a** BSE atomic number contrast images of the shocked monazite grains, the location of each SIMS U–Th–Pb analytical spot is marked on grains 10 and 11. **b** EBSD crystallographic orientation map, colored with an all Euler scheme, SIMS $^{207}Pb/^{206}Pb$ age measurements are marked for each spot. **c** EBSD grain misorientation map, which helps visualize the substructure of the grains by plotting each deviation angle of each pixel from the mean grain orientation, grain boundaries are defined as >10°. *Blue* domains are low strain, while *warm colors* represent higher degrees of misorientaiton, each SIMS spot is labeled with the calculated grain orientation spread (GOS) for the area of each analytical spot, see text for details of the calculation, uncalculated (uncalc.) values are from spots which crossed high-angle grain boundaries. Boundaries between adjacent pixels are also color-coded if they matched a specific misorientation axis and angle pair, within 5°, such as a known twin misorientation, a shocked zircon inclusion within grain 6 is colored with an IPF_z scheme. **d** EPMA Th Mα intensity maps, with measured Th concentrations (in ppm) for each SIMS spot. **e** Pole figures of monazite (010) colored with an all Euler scheme. Shock-deformed monazite grain (10) exhibits a combination of strained parent domains, including a high concentration of planar deformation bands (PDBs), and strain-free neoblasts. Monazite grain (11) in which the inner core of the grain has recrystallized to strain-free neoblasts and the other domains of the grain preserve PDBs and shock twins. Shock-deformed monazite (grain 6), which preserves PDBs, deformation twins, and a shocked zircon inclusion

The presence of deformation twins in strained domains from both samples is further evidence for crystal-plastic deformation. Twins found in both samples, including $(10\bar{1})$ and {212} in the ILG monazite, and $(10\bar{1})$,{110}, {212}, and two type two (irrational) twin planes (with rational shear directions (η1) in $[0\bar{1}\,\bar{1}]$ and $[\bar{1}\,\bar{1}0]$) in the Araguainha grains, are diagnostic of shock metamorphism (Erickson et al. 2016a). The difference in shock-twin types and abundances between the ILG and the AIM monazite grains may be a result of variable shock environments; further work is required to constrain the conditions of formation for specific twin orientations in monazite.

Monazite grains from Araguainha impact melt contain abundant planar microstructures composed of low-angle boundaries that accommodate as much as 11° of misorientation (e.g. Araguainha grain 7, appendix 4). The planar microstructures are consistent with PDBs described in detrital shocked monazite derived from the Vredefort

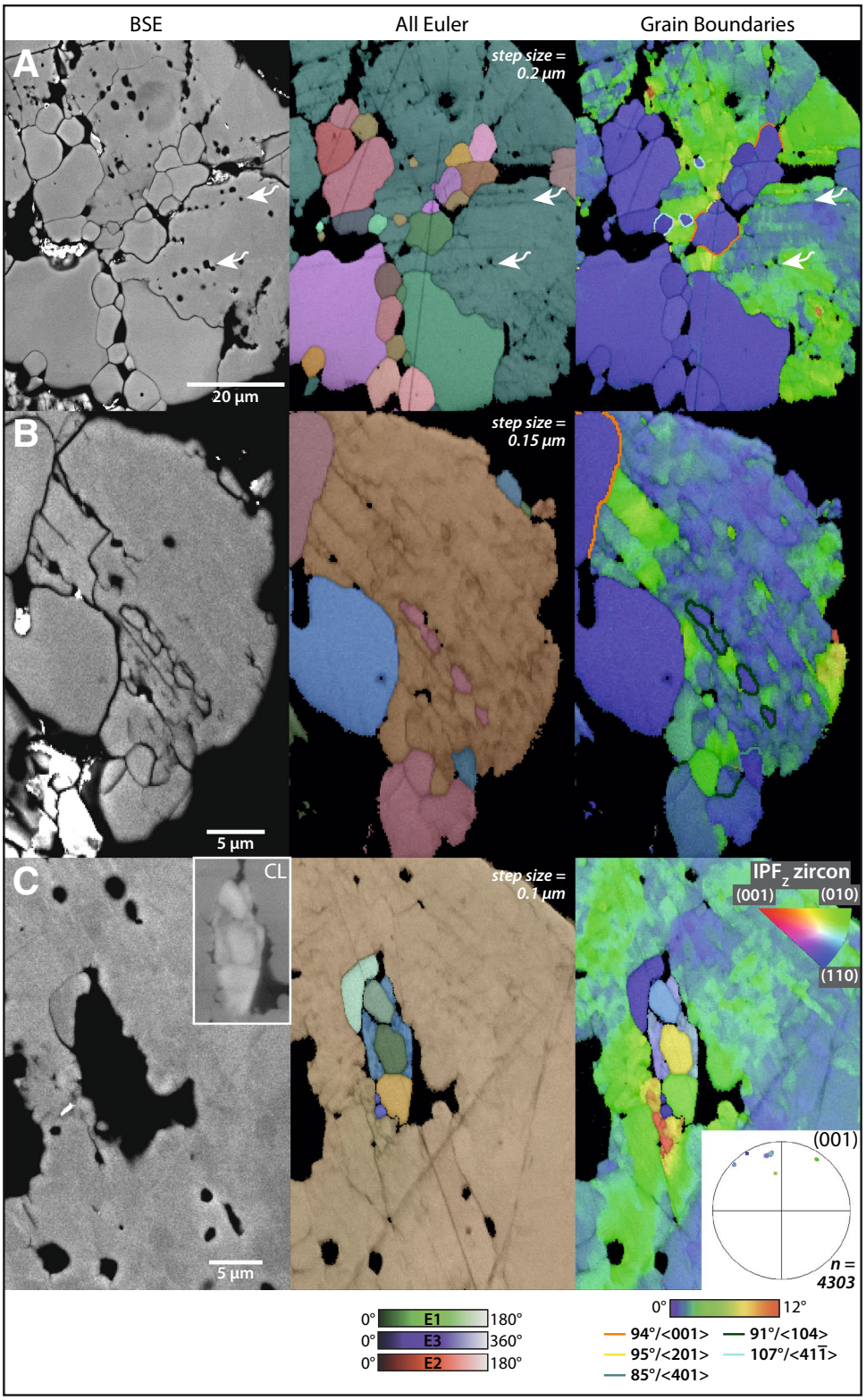

Fig. 5 High-resolution EBSD maps of regions of interest from shock-deformed monazite from sample ARA. BSE atomic number contrast images of each area of interest, with an inlaid CL image of the zircon inclusion from grain 6. EBSD crystallographic orientation maps colored with an all Euler scheme. EBSD grain misorientation maps, which help visualize the substructure of the grains by plotting the deviation angle of each pixel from the mean grain orientation, grain boundaries are defined as >10°. *Blue* domains are low strains, while *warm colors* represent higher degrees of misorientation. The boundaries between adjacent pixels are color-coded if they matched a specific misorientation axis and angle pair, within 5°, such as a known twin misorientation. The shocked zircon inclusion is colored with an IPF_z scheme. **a** Shock-deformed grain (10), with high-strain domains which are remnants of the host grain and low-strain neoblasts, many of which are found in orientations close to known deformation twins. *Curved arrows* point to some of the melt-bearing sub-planar fractures within the monazite. **b** Region of interest form grain 11, showing a combination of shock twins, high-strain PDBs and strain-free neoblasts. **c** A region of interest from grain 6, which contains a shocked zircon inclusion. Along the edge of the zircon, two domains (*light-blue* to *purple* in IPF_z) which contain plastic strain, are remnants of the parent grain, while four domains (*dark blue, royal blue, yellow* and *green* in IPF_z), which are unstrained, and non-systematically misoriented from one another, are neoblastic. Note the pole figure inlay for the orientation relationships within the zircon inclusion

Dome (Erickson et al. 2016a). In addition to PDBs, the AIM monazite grains contain sub-planar, low-angle boundary microstructures, along which occur trails of non-indexing (by EBSD), lower mean atomic number material that is darker in BSE images (e.g. Fig. 5a). The sub-planar trails appear similar to features described in zircon from the Vredefort Dome by Moser et al. (2011), which the authors interpreted as channels of injected melt.

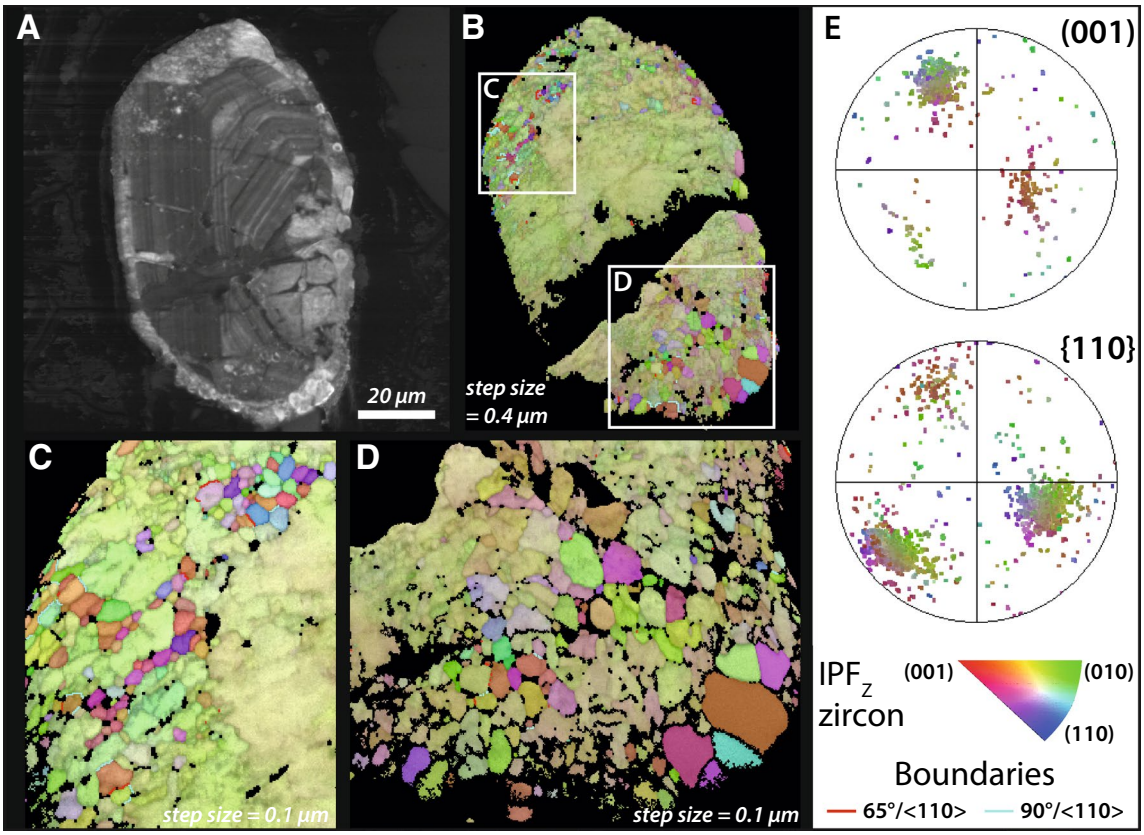

Fig. 6 A shock-deformed zircon from Araguainha impact melt sample ARA that contains granular subdomains. **a** CL image of the shocked zircon. **b** Orientation (IPF_z) and special boundary whole grain map of the shocked zircon, the plastically strained parent orientation is colored *yellow* to *green*. **c, d** High-resolution region of interest maps of domains with a high abundance of shock recrystallized zircon granules. Note that many of the granules have systematic grain boundaries of either 65°/<110> or 90°/<110>, which are consistent with granules which have formed from either shock {112} zircon twins or the reversion of high-pressure $ZrSiO_4$ polymorph reidite, respectively (Cavosie et al. 2016). **e** Pole figures of (001) and {110}, showing the systematic misorientation of the neoblastic domains, consistent with formation from either zircon shock twins or reversion from reidite

Monazite from both the ILG and the AIM contain randomly oriented subdomains which are either low-strain (ILG) or strain-free (AIM) and are highly misoriented relative to the host grain. We interpret these as neoblastic monazite formed by recrystallization (Erickson et al. 2015). Monazite neoblasts nucleate on deformation features, such as grain boundaries, within the strained parent monazite, indicating that stored strain energy has a key role in effectively lowering energy required to overcome the energy barrier for nucleation and growth of new grains via grain boundary migration. Through this process, newly grown, strain-free monazite grains are bounded by high-angle grain boundaries relative to parent monazite. Also, many of the neoblasts share specific crystallographic misorientation relationships with the host monazite that are consistent with known twin orientations for monazite (e.g. Figs. 4, 5a). The systematic orientations of monazite neoblasts, therefore, suggest that monazite neoblasts preferentially nucleate in orientations that minimize the host–neoblast interfacial energy, including syntaxially from pre-existing twins and host orientations. The formation of monazite neoblasts by dynamic recrystallization is not unique to shock metamorphism; similar neoblastic monazite has been shown to form in deformed rocks from the lower crust, in which, deformation occurs at high temperatures (Erickson et al. 2015). This process forms new monazite, free of inherited Pb, that can be used to date high-temperature deformation of the lower crust (Erickson et al. 2015).

We interpret the formation mechanism of neoblastic monazite during impact events to be similar to those in tectonic settings, and may not require hypervelocity shock pressures. The process of cannibalization of the host grain requires both strained lattice (as a result of shock) and high temperature to facilitate neoblast nucleation and growth, conditions present immediately after dissipation of the shock wave while post-shock temperatures are high. Monazite from the ILG experienced post-shock temperatures as high as 1300 °C (Gibson 2002).

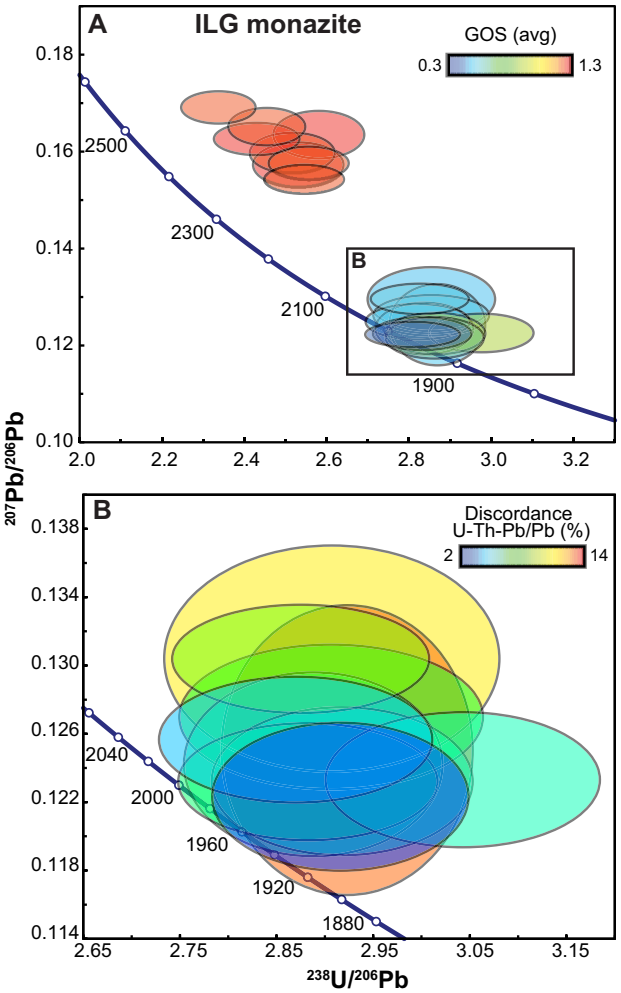

Fig. 7 U–Pb data for shocked monazite from sample 09SA06 from the ILG. **a** Tera–Wasserburg concordia diagram of all analyses, the spots are color-coded to average misorientation (as average grain orientation spread, GOS avg) calculated within the analyzed subgrain of each spot from the EBSD data (see appendix 1 for method). **b** Tera–Wasserburg concordia diagram of neoblastic domains, color-coded for discordance of the U–Th–Pb systematics. The analyses show a relative trend of discordance with increased common Pb. All error *ellipses* are 2σ

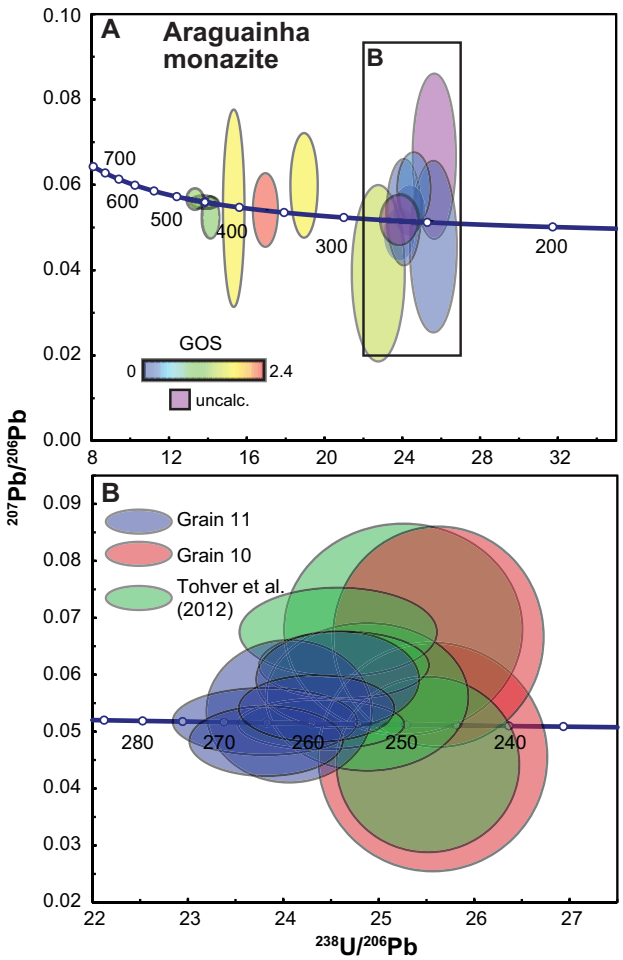

Fig. 8 U–Pb data for shocked monazite from sample ARA from the Araguainha melt rocks. **a** Tera–Wasserburg concordia diagram of all analyses, the spots are color-coded to misorientation (as grain orientation spread, GOS) calculated within the analytical area of each spot from the EBSD data. *Purple* analyses were uncalculated (uncalc.) because the spot crossed a grain boundary (see appendix 1 for method). **b** Tera–Wasserburg concordia diagram for neoblastic domains from grain 11 (*green spots*) and grain 10 (*red spots*) of this study and the youngest subgroup of Tohver et al. (2012) (*green spots*). Based on the textural evidence and the concordance of the analyses from grain 11, an impact age of 262 ± 3 Ma is proposed. All error *ellipses* are 2σ

Monazite grains from Araguainha were entrained within impact melt; while the formation temperature is unconstrained, at minimum, it would have been above the Araguainha granite liquidus (i.e., >700 °C), and likely much hotter, because impact melts can be superheated and reach temperatures >2000 °C (Grieve et al. 1977; Timms et al. 2017). Cooling rates from high post-shock temperatures are anticipated to occur over timescales within uncertainty of quantitative in situ SIMS U–Th–Pb dating, and therefore, the conditions which form neoblasts can be considered to be contemporaneous with impact shock events.

Constraints on shock conditions

Analysis of shock microstructures within zircon from the two samples allows evaluation of the P–T conditions experienced by shocked monazite (e.g. Erickson et al. 2016a). In the case of the ILG, the post-shock >1000 °C thermal pulse associated with granofels metamorphism (Gibson 2002), has erased the shock features in many of the major phases (e.g. PDFs in quartz); however, it has been estimated that the central part of the Vredefort Dome experienced shock pressure >30 GPa (Gibson

and Reimold 2005). The analyzed ILG zircon grains all contain {112} shock twins, a diagnostic shock microstructure (e.g. Moser et al. 2011; Timms et al. 2012, in press; Erickson et al. 2013a; Montalvo et al. 2017), which has been constrained to form by 20 GPa in both shock (Leroux et al. 1999) and static (Morozova 2015) experiments. Within partially metamict, dark CL cores in some domains of ILG zircon grains, cross-cutting, CL bright lamellae lie along the trace of indexed {112} twins on the polished surface. However, the bright lamellae share the crystallographic orientation of the parent grains and yield higher quality diffraction patterns compared to the CL dark core (Fig. 3). The bright lamellae are interpreted to be {112} shock twins that annealed back to the host zircon orientation. The core domains, therefore, preserve evidence of the former presence of the shock microstructures that were annealed after the shock pulse, either by high post-shock temperatures (cf. Gibson 2002; Timms et al. 2012) or subsequent tecotonometamorphic activity (Moser et al. 2011).

The provenance of the shocked monazite xenocrysts within AIM is more obscure. The impact melt is derived locally from adjacent basement granite (Silva et al. 2016) which is supported by the similar microstructural character of all analyzed monazite grains. Shocked zircon grains from Araguainha contain granular microstructure (cf. Bohor et al. 1993), which has been interpreted to form at higher impact pressures, after the formation of twins or transformation to reidite (Wittmann et al. 2006). Formation conditions of granular zircon are not experimentally calibrated and are, thus, poorly constrained; metamictization of the lattice could lower the P–T requirements for the formation of granular zircon. Systematic misorientation relationships between the neoblasts and shocked host (Fig. 6) are consistent with granular texture formation after twinning and reidite transformation (cf. Cavosie et al. 2016; Timms et al. 2017). Shock-generated reidite, from both experimental and natural studies, forms a systematic inter-crystalline misorientation relationship with the parent zircon, by which $<110>_{zircon}$ and $<110>_{reidite}$ are aligned and $[001]_{zircon}$ is aligned with the conjugate $<110>_{reidite}$ (Leroux et al. 1999; Reddy et al. 2015; Cavosie et al. 2015b; Erickson et al. 2017). It is, therefore, predicted that reversion of reidite to zircon produces domains with systematic 90°/<110> misorientation with the original host zircon orientation (Cavosie et al. 2016; Erickson et al. 2017; Timms et al. 2017). Thus, evidence for the former presence of reidite requires that the rocks achieved minimum shock pressure conditions of 30 GPa, based on shock experiments (Kusaba et al. 1985; Leroux et al. 1999). Because metamictization of zircon crystal structure inhibits the formation of reidite (Lang et al. 2008; Erickson et al. 2017; Timms et al. in press), the systematically misoriented granules, therefore, require the pre-existing zircon to have been crystalline, which supports our interpreted shock pressure.

Shocked monazite as an impact chronometer

These results show that determining the age of a shock event from deformed monazite is possible thorough characterization of specific microstructures that can be correlated to in situ U–Th–Pb ages. All analyses from strained domains at both sites are >10% discordant between the $^{207}Pb/^{206}Pb$ and $^{206}Pb/^{238}U$ systems. Ages from strained domains of the ILG range from 2537 to 2386 Ma; however, a regression from known age of the Vredefort impact, 2020 Ma, does not result in a meaningful upper intercept that corresponds to a known age for the basement of the Vredefort Dome. These results suggest that there is variable mobility of U, Th and radiogenic Pb during shock deformation (Fig. 9a). If correct, the implication is that shock deformation enhances the migration of both substitutional and interstitial ions. Partial age resetting resulting from the formation and migration of fast diffusion pathways created during the shock event may have resulted in a significant discordia array; subsequent deformation within the Kaapvaal Craton and/or modern Pb-loss has further modified the measured ages. Likewise, age data from shock-deformed monazite from bedrock of the Vredefort Dome (Flowers et al. 2003), and Vredefort-sourced detrital shocked monazite (Erickson et al. 2013b), that are dominated by lamellar microstructures, which we here interpret to be deformation twins, record ages from ca. 3180 to ca. 2157 Ma, and often do not represent meaningful geologic ages.

The Paleozoic age of the basement and impact event of the Araguainha structure (Tohver et al. 2012) complicates use of the $^{207}Pb/^{235}U$ system; however, $^{206}Pb/^{238}U$ ages from strained domains within Araguainha monazite range from 467 to 278 Ma. Measuring strain by EBSD from the area of the SHRIMP analytical spot reveals that the three oldest ages recorded in the AIM are preserved in the least strained domains of the parent grains (Fig. 8a). We, therefore, interpret the age spread within the U–Th–Pb systematics from the strained host domains to represent partial Pb-loss and mobility of U and Th as a result of fast diffusion pathways formed during the shock event. The subsequent reactivation of these hypothesized pathways by later deformation in the case of the ILG did not occur in grains from Araguainha.

The results of this study demonstrate that in situ analysis of shock-produced neoblastic monazite by SIMS can be used to date impact events. Neoblastic monazite domains from the ILG and AIM both yield concordant, young U–Pb ages, consistent with the age of the impact events constrained by independent means. The process of neoblast

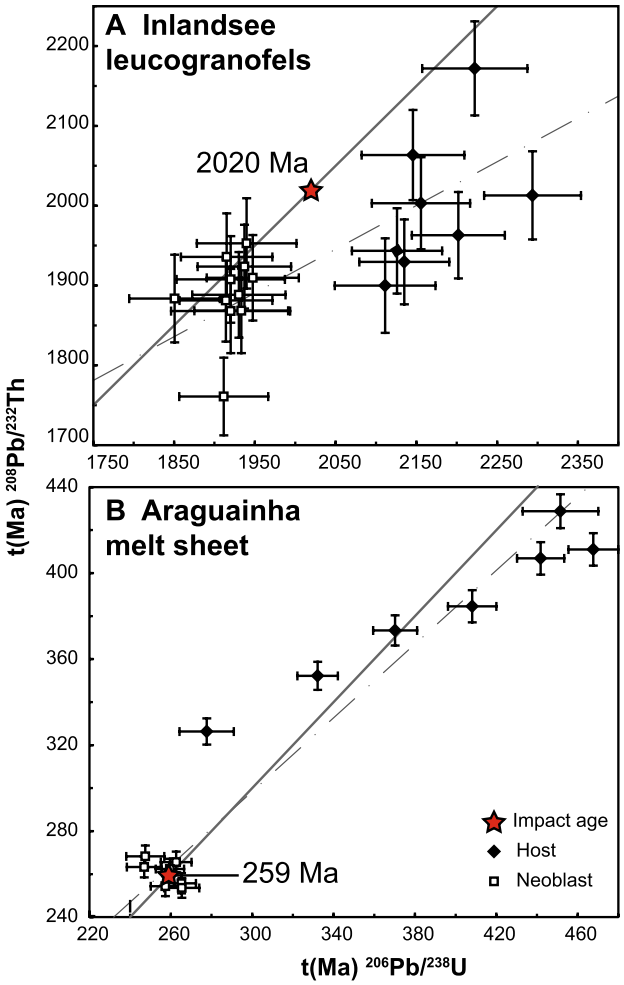

Fig. 9 Plots of $^{206}Pb/^{238}U$ vs. $^{208}Pb/^{232}Th$ ages for individual analyses from monazite from Vredefort and Araguainha, a one-to-one line is plotted as *solid grey*. **a** Variable Pb-loss between data collected from the deformed host and neoblast domains from the Vredefort ILG. While the 2020 Ma $^{207}Pb/^{206}Pb$ age is consistent with the Vredefort shock event, the U–Th systematics are significantly disturbed post-shock, however evenly, either the result of Kibaran regional metamorphism or modern Pb-loss. The post-impact disturbance may have significantly affected the systematics of the deformed host as well. **b** Disequilibrium between the U–Th systematics within the deformed host domains from the Araguainha impact structure is significant, while the systematics of the neoblasts are in agreement with one another, potentially due to the lack of post-shock deformation. All *error bars* are 2σ

growth, therefore, occurs free of inherited radiogenic Pb from the parent grain. Analyses of neoblastic monazite from the ILG are less than 10% discordant between the $^{207}Pb/^{206}Pb$ and $^{206}Pb/^{238}U$ systems, and the nine most concordant analyses record a weighted mean $^{207}Pb/^{206}Pb$ age of 2010 ± 15 Ma (MSWD = 0.84), within error of the 2020 Ma Vredefort impact event based on zircon from impact melt and recrystallized zircon (Kamo et al. 1996; Gibson et al. 1997; Moser 1997). The age from the neoblastic domains is also within error of the most concordant ID-TIMS $^{207}Pb/^{206}Pb$ age reported from granular monazite by Moser (1997), 2016 ± 7 Ma. The other grain analyzed by Moser (1997) is older (2090 ± 4 Ma), more discordant, and may represent a mixing age between the neoblasts and domains that retain pre-impact radiogenic Pb. This contrasts with U–Pb results from strained monazite grains, which preserve relatively discordant data with a wide age range, which do not necessarily correspond to a significant geologic date. The $^{207}Pb/^{206}Pb$ age from the ILG neoblastic monazite is consistent with the impact event; however, analysis of the $^{206}Pb/^{238}U$ and $^{208}Pb/^{232}Th$ systematics reveal open system behavior and, thus, yield younger ages (Fig. 9). Minor discordance within neoblastic domains from the ILG monazite is likely due to subsequent tectonic events in the Kaapvaal Craton after the Vredefort impact event. Deformation after the shock event at the Vredefort Dome has likely annealed some of the shock features within zircon from the ILG (e.g. Fig. 3), and has been shown to partially reset the U–Pb isotopic system in zircon from the ILG at ca. 1100 Ma (Moser et al. 2011), the age of mafic intrusions within the Kaapvaal (Reimold et al. 2000). Consideration of the subsequent geologic events is, therefore, also important when interpreting the age data from complex monazite grains, as they may cause partial resetting due to Pb mobility. In the case of the ILG, the post-shock deformation not only reactivated suspected fast diffusion pathways in the deformed parent domains but also caused minor Pb-loss within the neoblasts.

Neoblasts from AIM yield a concordia age of 259 ± 5 Ma (MSWD = 1.3), which is within error of the age of 255 ± 3 Ma reported by Tohver et al. (2012). However, if only analyses from grain 11 are considered, all of which are within uncertainty of concordia and have the lowest measured common Pb (<5% $F^{206}Pb$ %), they yield a slightly older and more precise age of 262 ± 3 Ma (MSWD = 0.88). The data from grain 10, which have been omitted, are from analytical spots on or near cracks and have the greatest measured common Pb and discordance between the U and Th systematics. Therefore, we suggest that the age of the Araguainha impact structure may be 262 ± 3 Ma, which is slightly older than the 255 ± 3 Ma determined previously, and highlight that further, careful analyses of neoblastic monazite domains could help to resolve the discrepancy.

Formation of neoblastic domains within monazite during shock appears to be a recrystallization process, whereby new monazite nucleates within the shock-deformed and strained lattice of the host and consumes the deformed lattice through the process of grain boundary migration. Similar deformation mechanisms have been identified in deformed monazite from the lower crust (Erickson et al. 2015), in zircon that has been tectonically strained (Piazolo et al. 2012) and shock-deformed (Cavosie et al. 2015a;

Timms et al. 2017) and in shocked baddeleyite (Darling et al. 2016). During the growth of neoblasts, incompatible ions are not incorporated into the newly formed lattice, and thus, the shock event and associated high temperature pulse set the age of the neoblasts.

Results from both the ILG and AIM highlight the value in directly linking quantitative microstructural analyses with in situ geochronologic analyses in shocked monazite to directly date impact structures, which is often challenging (Jourdan et al. 2009, 2012). Results from the Vredefort Dome also highlight the benefit of monazite, relative to other geochronometers, in terranes which have experienced subsequent geologic complexity. This is highlighted by the fact that although there is a ca. 1100 Ma overprint within the Vredefort Dome (Moser et al. 2011), the impact age is recorded in neoblastic domains from the ILG monazite. Furthermore, zircon analyzed from the ILG in this study only record crystal-plastic microstructures, which, in some cases, may be used to determine an impact age from a discordia trend (e.g. Moser et al. 2009, 2011) but in others may not (e.g. Schmieder et al. 2015; Cavosie et al. 2015a). As there is evidence of annealing of shock features in zircon, a discordia trend between the crystallization age of the zircon and the impact event at 2020 Ma may be obscured by subsequent Pb-loss, while the neoblastic monazite preserves the $^{207}Pb/^{206}Pb$ age of the impact event. Furthermore, monazite maintains a crystalline state and is not susceptible to metamictization (Meldrum et al. 1998; Seydoux-Guillaume et al. 2004). Therefore, while metamict softening of the zircon crystal lattice may inhibit the formation of shock features such as twins or reidite (Lang et al. 2008; Erickson et al. 2017; Timms et al. in press), monazite can unambiguously record the shock conditions, especially as a wide range of shock twins form in monazite, possibly due to varying conditions (Erickson et al. 2016a). These results show that monazite is subject to dynamic recrystallization at lower shock conditions than crystalline (i.e., non-metamict) zircon, and can, therefore, be used to date impact structures when other geochronometers may not record the impact age.

Conclusions

This study shows that monazite grains can record both diagnostic shock features and form neoblasts by dynamic recrystallization over a range of impact conditions. Shock microstructures within monazite, documented herein, include deformation twins and PDBs. Deformation twins were found as compound and/or type one twins in (001), (100), $(10\bar{1})$,{110}, {212}, and as type two (irrational) twin planes with rational shear directions (η1) in $[0\bar{1}\bar{1}]$ and $[\bar{1}\bar{1}0]$.Also, during the post-shock thermal pulse, neoblastic monazite may nucleate within the strained parent lattice and consume the strained lattice by grain boundary migration. Associated pressures have been constrained by microstructural analyses of zircon from the same samples. Shock twins within the ILG zircon record minimum impact pressures of 20 GPa, while systematically misoriented neoblasts within Araguainha zircon require minimum pressures of 30 GPa or higher.

In situ U–Th–Pb SIMS analyses of strained domains record discordant age arrays which may allow resolution of impact age, depending on subsequent geologic history of the structure. Analysis of monazite neoblasts from the ILG by SIMS yield a $^{207}Pb/^{206}Pb$ age of 2010 ± 15 Ma, consistent with the accepted 2020 Ma age of the Vredefort impact. Likewise, analysis of monazite neoblasts from the AIM yield a concordia age of 259 ± 5 Ma, which we interpret as the date of the Araguainha shock event. Because impact events are challenging to date (Jourdan et al. 2009), these results represent a significant advance in resolving impact ages. For example, of the 27 Precambrian impact structures (Earth Impact Database 2011), only four have precise ages (Jourdan et al. 2009). This study shows that coupling EBSD analyses of monazite microstructures with targeted high-resolution U–Th–Pb analyses either by SIMS or LA-ICPMS, offers another method to date impact structures, including Precambrian (e.g. Vredefort) and Phanerozoic (e.g. Araguainha) impact structures, even those that have experienced subsequent tectonic deformation.

Acknowledgements TME acknowledges financial support from an International Post-Graduate Research Grant from Curtin University Office of Research and Development and from the ARC Core to Crust Fluid System COE. The ARC (LE130100053), Curtin University, University of Western Australia and CSIRO are acknowledged for funding the Tescan Mira3 FEG-SEM housed in the John De Laeter Centre's Microscopy and Microanalysis Facility. The authors would like to thank Ben Wade at Adelaide Microscopy for collecting the EPMA maps. We would like to thank two anonymous reviewers and editor Prof. O. Müntener for the detailed and insightful comments that have substantially improved this manuscript.

References

Armstrong RA, Lana C, Uwe Reimold W, Gibson RL (2006) SHRIMP zircon age constraints on Mesoarchean crustal development in the Vredefort dome, central Kaapvaal Craton, South Africa. Geol Soc Am Spec Pap 405:233–253. doi:10.1130/2006.2405(13)

Bischoff AA, Mayer JJ, Voors WA, Retief PF (1999) Geology of the Vredefort Dome. Council for Geoscience, Pretoria

Bohor BF, Betterton WJ, Krogh TE (1993) Impact-shocked zircons: discovery of shock-induced textures reflecting increasing degrees of shock metamorphism. Earth Planet Sci Lett 119:419–424. doi:10.1016/0012-821X(93)90149-4

Buick IS, Clark C, Rubatto D, Hermann J, Pandit M, Hand M (2010) Constraints on the Proterozoic evolution of the Aravalli–Delhi Orogenic belt (NW India) from monazite geochronology and

mineral trace element geochemistry. Lithos 120:511–528. doi:10.1016/j.lithos.2010.09.011

Catlos EJ (2013) Versatile Monazite: resolving geological records and solving challenges in materials science: generalizations about monazite: implications for geochronologic studies. Am Mineral 98:819–832. doi:10.2138/am.2013.4336

Cavosie AJ, Quintero RR, Radovan HA, Moser DE (2010) A record of ancient cataclysm in modern sand: Shock microstructures in detrital minerals from the Vaal River, Vredefort Dome, South Africa. Geol Soc Am Bull 122:1968–1980. doi:10.1130/b30187.1

Cavosie AJ, Erickson TM, Timms NE, Reddy SM, Talavera C, Montalvo SD, Pincus MR, Gibbon RJ, Moser D (2015a) A terrestrial perspective on using ex situ shocked zircons to date lunar impacts. Geology 43:999–1002. doi:10.1130/g37059.1

Cavosie AJ, Erickson TM, Timms NE (2015b) Nanoscale records of ancient shock deformation: Reidite (ZrSiO4) in sandstone at the Ordovician Rock Elm impact crater. Geology 43:315–318. doi:10.1130/g36489.1

Cavosie AJ, Timms NE, Erickson TM, Hagerty JJ, Hörz F (2016) Transformations to granular zircon revealed: Twinning, reidite, and ZrO2 in shocked zircon from Meteor Crater (Arizona, USA). Geology 44:703–706. doi:10.1130/g38043.1

Cavosie AJ, Erickson TM, Montalvo P, Prado D, Cintron N, Gibbon RJ (in press) The Rietputs Formation in South Africa: a Pleistocene fluvial archive of meteorite impact unique to the Kaapvaal craton. In: Moser DE, Corfu F, Reddy SM, Darling J, Tait K (eds) Microstructural Geochronology; Lattice to Atom-Scale Records of Planetary Evolution. AGU Monograph. AGU-Wiley, New Jersey

D'Abzac F-X, Seydoux-Guillaume A-M, Chmeleff J, Datas L, Poitrasson F (2012) In situ characterization of infrared femtosecond laser ablation in geological samples. Part A: the laser induced damage. J Anal At Spectrom 27:99–107. doi:10.1039/C1JA10153F

Darling JR, Moser DE, Barker IR, Tait KT, Chamberlain KR, Schmitt AK, Hyde BC (2016) Variable microstructural response of baddeleyite to shock metamorphism in young basaltic shergottite NWA 5298 and improved U–Pb dating of Solar System events. Earth Planet Sci Lett 444:1–12. doi:10.1016/j.epsl.2016.03.032

Deutsch A, Schärer U (1990) Isotope systematics and shock-wave metamorphism: I. U–Pb in zircon, titanite and monazite, shocked experimentally up to 59 GPa. Geochim Cosmochim Acta 54:3427–3434. doi:10.1016/0016-7037(90)90295-V

Engelhardt WV, Matthäi SK, Walzebuck J (1992) Araguainha impact crater, Brazil. I. The interior part of the uplift. Meteoritics 27:442–457. doi:10.1111/j.1945-5100.1992.tb00226.x

Earth Impact Database (2011) Planetary and space science centre. University of New Brunswick. http://www.passc.net/EarthImpactDatabase/. Accessed 2017

Erickson TM, Cavosie AJ, Moser DE, Barker IR, Radovan HA (2013a) Correlating planar microstructures in shocked zircon from the Vredefort Dome at multiple scales: crystallographic modeling, external and internal imaging, and EBSD structural analysis. Am Mineral 98:53–65. doi:10.2138/am.2013.4165

Erickson TM, Cavosie AJ, Moser DE, Barker IR, Radovan HA, Wooden J (2013b) Identification and provenance determination of distally transported, Vredefort-derived shocked minerals in the Vaal River, South Africa using SEM SHRIMP-RG techniques. Geochim Cosmochim Acta 107:170–188. doi:10.1016/j.gca.2012.12.008

Erickson TM, Pearce MA, Taylor RJM, Timms NE, Clark C, Reddy SM, Buick IS (2015) Deformed monazite yields high-temperature tectonic ages. Geology 43:383–386. doi:10.1130/g36533.1

Erickson TM, Cavosie AJ, Pearce MA, Timms NE, Reddy SM (2016a) Empirical constraints on shock features in monazite using shocked zircon inclusions. Geology 44:635–638. doi:10.1130/g37979.1

Erickson TM, Reddy SM, Timms NE, Pearce MA, Taylor RJM, Clark C, Buick IS (2016b) Deformed monazite yields high-temperature tectonic ages: REPLY. Geology 44:e378. doi:10.1130/g37474y.1

Erickson TM, Pearce MA, Reddy SM, Timms NE, Cavosie AJ, Bourdet J, Rickard WDA, Nemchin AA (2017) Microstructural constraints on the mechanisms of the transformation to reidite in naturally shocked zircon. Contrib Mineral Petrol 172:6. doi:10.1007/s00410-016-1322-0

Fletcher IR, McNaughton NJ, Davis WJ, Rasmussen B (2010) Matrix effects and calibration limitations in ion probe U–Pb and Th–Pb dating of monazite. Chem Geol 270:31–44. doi:10.1016/j.chemgeo.2009.11.003

Flowers RM, Moser DE, Hart R (2003) Evolution of the Amphibolite-Granulite facies transition exposed by the Vredefort impact structure, Kaapvaal Craton, South Africa. J Geol 111:455–470. doi:10.1086/375282

French BM, Koeberl C (2010) The convincing identification of terrestrial meteorite impact structures: what works, what doesn't, and why. Earth Sci Rev 98:123–170. doi:10.1016/j.earscirev.2009.10.009

Gibson RL (2002) Impact-induced melting of Archean granulites in the Vredefort Dome, South Africa. I: anatexis of metapelitic granulites. J Metamorph Geol 20:57–70. doi:10.1046/j.0263-4929.2001.00358.x

Gibson RL, Reimold WU (2005) Shock pressure distribution in the Vredefort impact structure, South Africa. Geol Soc Am Spec Pap 384:329–349. doi:10.1130/0-8137-2384-1.329

Gibson RL, Armstrong RA, Reimold WU (1997) The age and thermal evolution of the Vredefort impact structure: a single-grain U·Pb zircon study. Geochim Cosmochim Acta 61:1531–1540. doi:10.1016/S0016-7037(97)00013-6

Gibson RL, Uwe Reimold W, Stevens G (1998) Thermal-metamorphic signature of an impact event in the Vredefort dome, South Africa. Geology 26:787–790. doi:10.1130/0091-7613(1998)026<0787:tmsoai>2.3.co;2

Grieve RA, Dence M, Robertson P (1977) Cratering processes-As interpreted from the occurrence of impact melts. In: Roddy DJ, Pepin RO, Merril RB (eds) Impact and explosion cratering: Planetary and terrestrial implications. Paragamon, New York, pp 791–814

Hart R, Moser D, Andreoli M (1999) Archean age for the granulite facies metamorphism near the center of the Vredefort structure, South Africa. Geology 27:1091–1094. doi:10.1130/0091-7613(1999)027<1091:aaftgf>2.3.co;2

Hay RS, Marshall DB (2003) Deformation twinning in monazite. Acta Mater 51:5235–5254. doi:10.1016/s1359-6454(03)00305-7

Ivanov BA (2005) Numerical modeling of the largest terrestrial meteorite craters. Sol Syst Res 39:381–409. doi:10.1007/s11208-005-0051-0

Jourdan F, Renne PR, Reimold WU (2009) An appraisal of the ages of terrestrial impact structures. Earth Planet Sci Lett 286:1–13. doi:10.1016/j.epsl.2009.07.009

Jourdan F, Reimold WU, Deutsch A (2012) Dating terrestrial impact structures. Elements 8:49–53 doi:10.2113/gselements.8.1.49

Kamo SL, Reimold WU, Krogh TE, Colliston WP (1996) A 2.023 Ga age for the Vredefort impact event and a first report of shock metamorphosed zircons in pseudotachylitic breccias and Granophyre. Earth Planet Sci Lett 144:369–387. doi:10.1016/S0012-821X(96)00180-X

Kusaba K, Syono Y, Kikuchi M, Fukuoka K (1985) Shock behavior of zircon: phase transition to scheelite structure and decomposition. Earth Planet Sci Lett 72:433–439. doi:10.1016/0012-821X(85)90064-0

Lana C, Filho CRS, Marangoni YR, Yokoyama E, Trindade RIF, Tohver E, Reimold WU (2007) Insights into the morphology, geometry, and post-impact erosion of the Araguainha peak-ring structure, central Brazil. Geol Soc Am Bull 119:1135–1150. doi:10.1130/b26142.1

Lana C, Filho CRS, Marangoni YR, Yokoyama E, Trindade RIF, Tohver E, Reimold WU (2008) Structural evolution of the 40 km wide Araguainha impact structure, central Brazil. Meteorit Planet Sci 43:701–716. doi:10.1111/j.1945-5100.2008.tb00679.x

Lang M, Zhang F, Lian J, Trautmann C, Neumann R, Ewing RC (2008) Irradiation-induced stabilization of zircon (ZrSiO4) at high pressure. Earth Planet Sci Lett 269:291–295. doi:10.1016/j.epsl.2008.02.027

Langenhorst F, Deutsch A (2012) Shock metamorphism of minerals. Elements 8:31–36 doi:10.2113/gselements.8.1.31

Leroux H, Reimold WU, Koeberl C, Hornemann U, Doukhan JC (1999) Experimental shock deformation in zircon: a transmission electron microscopic study. Earth Planet Sci Lett 169:291–301. doi:10.1016/S0012-821X(99)00082-5

Machado R, Lana C, Stevens G, Filho CRS, Reimold WU, McDonald I (2009) Generation, mobilization and crystallization of impact-induced alkali-rich melts in granitic target rocks: evidence from the Araguainha impact structure, central Brazil. Geochim Cosmochim Acta 73:7183–7201. doi:10.1016/j.gca.2009.08.029

Meldrum A, Boatner LA, Weber WJ, Ewing RC (1998) Radiation damage in zircon and monazite. Geochim Cosmochim Acta 62:2509–2520. doi:10.1016/S0016-7037(98)00174-4

Melosh J (1989) Impact cratering: a geologic process. In: Oxford Monographs on Geology and Geophysics 11, Oxford University Press, New York, 253 p

Montalvo SD, Cavosie AJ, Erickson TM, Talavera C (2017) Fluvial transport of impact evidence from cratonic interior to passive margin: vredefort-derived shocked zircon on the Atlantic coast of South Africa. Am Mineral 102. doi:10.2138/am-2017-5857CCBYNCND

Morozova I (2015) Strength study of zircon under high pressure, Thesis. The University of Western Ontario, 112 p

Moser DE (1997) Dating the shock wave and thermal imprint of the giant Vredefort impact, South Africa. Geology 25:7–10. doi:10.1130/0091-7613(1997)025<0007:dtswat>2.3.co;2

Moser DE, Flowers RM, Hart RJ (2001) Birth of the Kaapvaal tectosphere 3.08 billion years ago. Science 291:465–468. doi:10.1126/science.291.5503.465

Moser DE, Davis WJ, Reddy SM, Flemming RL, Hart RJ (2009) Zircon U–Pb strain chronometry reveals deep impact-triggered flow. Earth Planet Sci Lett 277:73–79. doi:10.1016/j.epsl.2008.09.036

Moser DE, Cupelli CL, Barker IR, Flowers RM, Bowman JR, Wooden J, Hart JR (2011) New zircon shock phenomena and their use for dating and reconstruction of large impact structures revealed by electron nanobeam (EBSD, CL. EDS) isotopic U–Pb (U–Th)/He analysis of the Vredefort dome. Can J Earth Sci 48:117–139. doi:10.1139/e11-011

Niihara T, Kaiden H, Misawa K, Sekine T, Mikouchi T (2012) U–Pb isotopic systematics of shock-loaded and annealed baddeleyite: implications for crystallization ages of Martian meteorite shergottites. Earth Planet Sci Lett 341–344:195–210. doi:10.1016/j.epsl.2012.06.002

Piazolo S, Austrheim H, Whitehouse M (2012) Brittle-ductile microfabrics in naturally deformed zircon: Deformation mechanisms and consequences for U–Pb dating. Am Mineral 97:1544–1563. doi:10.2138/am.2012.3966

Reddy SM, Timms NE, Pantleon W, Trimby P (2007) Quantitative characterization of plastic deformation of zircon and geological implications. Contrib Mineral Petrol 153:625–645. doi:10.1007/s00410-006-0174-4

Reddy SM, Johnson TE, Fischer S, Rickard W, Taylor RJM (2015) Precambrian redite discovered in shocked zircon from the Stac Fada impactite, Scotland. Geology 43:899–902. doi:10.1130/g37066.1

Reimold WU, Pybus GQJ, Kruger FJ, Layer PW, Koeberl C (2000) The Anna's Rust Sheet and related gabbroic intrusions in the Vredefort Dome-Kibaran magmatic event on the Kaapvaal Craton and beyond? J Afr Earth Sci 31:499–521. doi:10.1016/S0899-5362(00)80004-4

Schärer U, Deutsch A (1990) Isotope systematics and shock-wave metamorphism: II. U–Pb and Rb–Sr in naturally shocked rocks; the Haughton Impact Structure, Canada. Geochim Cosmochim Acta 54:3435–3447. doi:10.1016/0016-7037(90)90296-W

Schmieder M, Tohver E, Jourdan F, Denyszyn SW, Haines PW (2015) Zircons from the Acraman impact melt rock (South Australia): Shock metamorphism, U–Pb and 40Ar/39Ar systematics, and implications for the isotopic dating of impact events. Geochim Cosmochim Acta 161:71–100. doi:10.1016/j.gca.2015.04.021

Seydoux-Guillaume A-M, Wirth R, Deutsch A, Schärer U (2004) Microstructure of 24–1928 Ma concordant monazites; implications for geochronology and nuclear waste deposits. Geochim Cosmochim Acta 68:2517–2527. doi:10.1016/j.gca.2003.10.042

Seydoux-Guillaume A-M, Freydier R, Poitrasson F, D'Abzac F-x, Wirth R, Datas L (2010) Dominance of mechanical over thermally induced damage during femtosecond laser ablation of monazite. Eur J Mineral 22:235–244. doi:10.1127/0935-1221/2010/0022-2001

Silva D, Lana C, de Souza Filho CR (2016) Petrographic and geochemical characterization of the granitic rocks of the Araguainha impact crater, Brazil. Meteorit Planet Sci 51:443–467. doi:10.1111/maps.12601

Stacey JS, Kramers JD (1975) Approximation of terrestrial lead isotope evolution by a two-stage model. Earth Planet Sci Lett 26(2):207–221. doi:10.1016/0012-821X(75)90088-6

Stepto D (1990) The geology and gravity field in the central core of the Vredefort structure. Tectonophysics 171:75–103. doi:10.1016/0040-1951(90)90091-L

Stöffler D, Langenhorst F (1994) Shock metamorphism of quartz in nature and experiment: I. Basic observation and theory*. Meteoritics 29:155–181. doi:10.1111/j.1945-5100.1994.tb00670.x

Timms NE, Reddy SM, Healy D, Nemchin AA, Grange ML, Pidgeon RT, Hart R (2012) Resolution of impact-related microstructures in lunar zircon: a shock-deformation mechanism map. Meteorit Planet Sci 47:120–141. doi:10.1111/j.1945-5100.2011.01316.x

Timms NE, Erickson TM, Pearce MA, Cavosie AJ, Schmieder M, Tohver E, Reddy SM, Zanetti MR, Nemchin AA, Wittmann A (2017) A pressure-temperature phase diagram for zircon at extreme conditions. Earth Sci Rev 165:185–202 doi:10.1016/j.earscirev.2016.12.008

Timms NE, Healy D, Erickson TM, Nemchin AA, Pearce MA, Cavosie AJ (in press) Role of elastic anisotropy in the development of deformation microstructures in zircon. In: Moser DE, Corfu F, Reddy SM, Darling J, Tait K (eds) Microstructural geochronology; lattice to atom-scale records of planetary evolution. AGU Monograph. AGU-Wiley

Tohver E, Lana C, Cawood PA, Fletcher IR, Jourdan F, Sherlock S, Rasmussen B, Trindade RIF, Yokoyama E, Souza Filho CR, Marangoni Y (2012) Geochronological constraints on the age of a Permo–Triassic impact event: U–Pb and 40Ar/39Ar results for the 40 km Araguainha structure of central Brazil. Geochim Cosmochim Acta 86:214–227. doi:10.1016/j.gca.2012.03.005

Wawrzenitz N, Krohe A, Rhede D, Romer RL (2012) Dating rock deformation with monazite: The impact of dissolution precipitation creep. Lithos 134–135:52–74. doi:10.1016/j.lithos.2011.11.025

Wittmann A, Kenkmann T, Schmitt RT, Stöffler D (2006) Shock-metamorphosed zircon in terrestrial impact craters. Meteorit Planet Sci 41:433–454. doi:10.1111/j.1945-5100.2006.tb00472.x